This is a preprint, the final version is subject to change, of the American Mineralogist (MSA)
Cite as Authors (Year) Title. American Mineralogist, in press.
DOI: http://dx.doi.org/10.2138/am-2018-6288

1 **Revision 4**

2

3 **A mineralogical archive of the biogeochemical sulfur cycle preserved in the subsurface of the**
4 **Río Tinto system**

5

6 David C Fernández-Remolar[1,*], Neil Banerjee[2], David Gómez-Ortiz[3], Matthew Izawa[4], and Ricardo
7 Amils[5, 6].

8

9 [1]Department of Computer Science, Electrical and Space Engineering, Luleå University of
10 Technology, Luleå, Sweden

11 [2]Centre for Planetary Science and Exploration (CPSX), Department of Earth Sciences, University of
12 Western Ontario, 1151 Richmond Street, London, Ontario, Canada, N6A 5B7

13 [3]ESCET-Área de Geología, Universidad Rey Juan Carlos, 28933 Móstoles, Madrid, Spain

14 [4]Institute for Planetary Materials, Okayama University, Misasa, Tottori, 682-0193, Japan

15 [5]Planetology and Habitability Department, Center of Astrobiology (INTA-CSIC), Torrejón de Ardoz,
16 28850 Madrid, Spain

17 [6]Centro de Biología Molecular Severo Ochoa (CSIC-UAM), Universidad Autónoma de Madrid,
18 Cantoblanco, 28049 Madrid, Spain

19

20

This is a preprint, the final version is subject to change, of the American Mineralogist (MSA)
Cite as Authors (Year) Title. American Mineralogist, in press.
DOI: http://dx.doi.org/10.2138/am-2018-6288

ABSTRACT

The search for extinct and extant life on Mars is based on the study of biosignatures that could be preserved under Mars-like, extreme conditions that are replicated in different terrestrial analog environments. The mineral record in the subsurface of the Río Tinto system is one example of a Mars analog site that has been exposed to weathering conditions, including the biogeochemical activity of Fe and S chemolithotrophic bacteria, for millions of years. The SEM-EDAX analysis of different samples recovered in the Peña de Hierro area from four boreholes, ranging from 166 to 610 meters in depth, has provided the identification of microbial structures that have affected a suite of hydrothermal minerals (~ 345 Ma) as well as minerals likely produced by biological activity in more recent times (< 7 Ma). The hydrothermal minerals correspond to reduced sulfur or sulfate-bearing compounds (e.g., pyrite and barite) that are covered by bacilli- or filamentous-like microbial structures and/or secondary ferrous carbonates (e.g., siderite) with laminar to spherical structures. The secondary iron carbonates can be in direct contact or above an empty interphase with the primary hydrothermal minerals following a wavy to bent contact. Such an empty interphase is usually filled with nanoscale, straight filamentous structures that have a carbonaceous composition. The occurrence of a sulfur and iron chemolithotrophic community in the Río Tinto basement strongly suggests that the association between sulfur-bearing minerals, dissolution scars and secondary minerals of biological origin is a complex process involving the microbial attack on mineral surfaces by sulfur reducing bacteria followed by the precipitation of iron-rich carbonates. In this scenario, iron sulfide compounds such as pyrite would act as electron donors under microbial oxidation, while sulfate minerals such as barite would act as electron acceptors through sulfate reduction. Furthermore, the formation of siderite would have resulted from carbonate biomineralization of iron chemoheterotrophic organims or other microorganisms that concentrate carbonate through metabolic pathways. Although the distribution of the mineral biosignatures at depth clearly follows a redox gradient, they show some irregular allocation underground, suggesting that the geochemical conditions governing the microbial activity are affected by local changes associated with the fracturing pattern of the Río Tinto basement. The abundance of sulfur- and iron-bearing minerals in

the Mars crust suggests that the Río Tinto mineral biosignatures can be useful in the search for extant and extinct subsurface life on the red planet.

Keywords: Rio Tinto, Biomineralization, Subsurface, Mars

INTRODUCTION

The biogeochemical cycling of elements on Earth has occurred for over four billion years (Knoll et al. 2012). Through such a long-term interaction of microbes with minerals, the geosphere has recorded very different components, including structures, fossil bodies, minerals, isotopic fractionation, organic compounds or biomolecules, that unequivocally evidence a biological origin. While biomolecules and organic compounds provide taxonomic, phylogenic, ecological and/or metabolic information for the identification of living forms that have produced them (Brocks and Summons 2003), mineral biosignatures provide clues about the metabolic pathways and biogeochemical cycles occurring in Earth's natural systems (Banfield et al. 2001). In this regard, some minerals produced under adverse thermodynamic conditions can form as by-products of microbial metabolism and can be robust biosignatures. This is the case for the microbial-induced precipitation of siderite by local changes of pH occurring at the microscale under the extremely acidic conditions of the Mars terrestrial analog of Río Tinto (Fernández-Remolar et al. 2012). Consequently, when mineral stability is considered together with geochemical conditions and biological activity in any geochemical system, it can be used as a good reference for identifying biological activity through mineral diversity. Furthermore, if such geological systems have been identified as suitable analogs of Mars, then the mineral record resulting from interactions with microbiota can be used as conceptual tools to search for life on the red planet.

In this paper, we show how the mineral record has captured the microbial activity in the basement rock of the Río Tinto Mars analog in the Peña de Hierro area during the last 25 millions of years. This has resulted through the synthesis of the knowledge generated in the last two decades through multidisciplinary studies involving the mineralogy, microbiology, geobiology and geochemistry of such an extreme environment (Fernández-Remolar et al., 2005, 2008, 2011). As one of the main results shows, it has been possible to build strong links between the metabolism of sulfur and iron bacteria (Fernández-Remolar et al. 2008) and the dynamics of sulfur-bearing minerals occurring in the subsurface. Therefore, as a reversed exercise, the formation versus the destruction of iron and sulfur minerals has provided essential information to understand the microbial processes that have been recorded in the Río Tinto basement on geological time scales. Therefore, such a methodological approach can provide the sulfur and iron mineral cycling to be used as a tool for unlocking geochemical processes and determining whether such cycles were sustained by a putative microbiota on Mars.

GEOLOGICAL SETTINGS

The Río Tinto river is a ca. 100 km long river containing a high concentration of heavy metals in solution and extremely acidic conditions (i.e., pH < 3 and Eh > 400 mV). The river is partially sourced by acidic springs located in the Peña de Hierro area, Huelva, southwestern Spain (Fernández-Remolar et al. 2005, 2008). This corresponds to an important mining operation area that comprises the Río Tinto mine district, which is one of the world's largest massive and stockwork sulfide deposits. These mining sites have a long history of activity over the last ca. 5000 years (Davis et al. 2000). Such activity has exposed large outcrops of massive and stockwork sulfides to meteoric water, thereby accelerating metal sulfide oxidation. However, it is a well-known fact that acid mine drainage (AMD) originates from sulfide mineral oxidation catalyzed by iron-oxidizing bacteria that release acid as a by-product of active metabolism (Nordstrom et al. 2000). Consequently, the extreme

conditions of the Río Tinto have been explained so far as a contamination process related to the long mining activity taking place within its catchment area (Davis et al., 2000). However, continuous exploration of the geological, geophysical and microbiological conditions in the Río Tinto area over the last 15 years has provided data suggesting that the acidic conditions of the river are not a consequence of the mining activity alone but have remained constant over the last 20 Ma (Fernández-Remolar et al. 2005; Gómez-Ortiz et al. 2014).

Peña de Hierro is an important sulfide ore mining area located at the contact between two different tectonic units belonging to the Iberian Pyrite Belt (IPB). The IPB is a 250 km long and ca. 60 km wide geological unit that forms the northernmost paleogeographic division of the South-Portuguese zone of the Variscan Iberian Massif (Leistel et al. 1998). The presence of rocks formed in an oceanic crust separating the South-Portuguese zone from the rest of the Iberian Massif suggests an exotic origin of this zone relative to the Gondwanan-affinity Iberian Autochthon (Quesada 1991). The stratigraphic record of the Iberian Pyrite Belt can be summarized in three sequences: 1) a Phyllite-Quartzite (PQ) Group of Frasnian to Late Famennian age (Oliveira 1990); 2) a bimodal volcano-sedimentary complex (VSC) ranging in age from Late Famennian to the first part of the Late Viséan (~ 375-340 Ma), where different metallic ores were formed in response to hydrothermalism and tectonism during the pre-collisional stages of the Variscan orogeny (Leistel et al. 1998; Quesada 1998); and 3) a younger Culm Group (<335 Ma) with turbiditic characteristics (Late Viséan onwards) that records syn-orogenic foreland basin deposition during the collisional stage of the Variscan orogeny (Leistel et al. 1998; Quesada 1998). The overall structure of the IPB, as well as that of the entire South-Portuguese zone, corresponds to a huge imbricate fan of thrust sheets rooted in the middle crust (Quesada 1998). Location of the basal detachment within the Late Devonian PQ Group is the reason why no rocks older than this are exposed in the entire region. Significantly, the imbricate thrust structure contains an important oblique-slip component, which is due to the oblique conditions under which the Variscan collision occurred in this part of the orogeny (Quesada 1991, 1998).

125

126 The subsurface exploration of the Río Tinto basement in Peña de Hierro has been performed under the
127 umbrella of two main research projects focused on the astrobiology potential of the Río Tinto extreme
128 acidic system. During 2003 and 2004, the MARTE project (Mars Analog and Technology
129 Experiment) simulated a robotic drilling mission to search for subsurface life on Mars (Stoker et al.
130 2008). For such a purpose, the Río Tinto basement was sampled through different boreholes that
131 principally targeted volcano-sedimentary deposits hosting the metallic orebody. As a result, a total of
132 350 m of cores were recovered from three drilling targets named BH1, BH4 and BH8 (Fernández-
133 Remolar et al. 2008) that provided the source of information to determine the microbial activity and
134 biogeochemical cycles in the subsurface. In this regard, Fernández-Remolar et al. (2008) identified
135 different subsurface habitats that were characterized by microbial processes controlling the pH and Eh
136 in the Río Tinto Variscan basement.

137

138 In the following years, 2011 to 2014, the IPBSL (Iberian Pyrite Belt Subsurface Life) project was the
139 second effort to explore the Río Tinto basement that examined the subsurface of the extreme system
140 through approximately 1000 m of cores. During 2011, a complete geophysical survey was carried out
141 to detect the occurrence of groundwater as well as the possible location of unknown deep massive
142 and/or stockwork sulfide bodies in the area. Two different methods, Electrical Resistivity
143 Tomography (ERT) and Time Domain ElectroMagnetics (TDEM) (Gómez-Ortiz et al. 2014), were
144 used to sound the Variscan basement. As the presence of both water and metallic bodies greatly
145 modify the electrical properties of the rocks, the methods are especially well suited to the proposed
146 targets. ERT profiles reaching an investigation depth of ca. 200 m (Gómez-Ortiz et al. 2014) revealed
147 the occurrence of two different geoelectrical units: an upper medium-to-high resistivity unit (2000-
148 2500 ohm·m) mimicking the morphology and distribution of the Tournaisian metarhyolites of the
149 VSC that outcrop in the northern (hanging wall) part of Peña de Hierro area, and a lower, low
150 resistivity unit fitting the younger Culm Group that occurs in the southern (foot wall) area. The

boundary between both units is defined by a narrow zone dipping north that fits the location of a mapped major thrust structure that puts into contact the Tournaisian VSC unit and the Culm Group. The massive sulfide ore body mined out at Peña de Hierro was one of several structural imbricates located along this major tectonic fault.

As discussed by Gómez-Ortiz et al. (2014), such a geophysical survey was used to select different drilling targets, based on the distribution of aquifers and metallic orebodies that are the energy source for the microbial community inhabiting the Río Tinto basement. The survey resulted in the selection of two different drilling locations, named BH10 and BH11, for sample collection in the volcano-sedimentary complex hosting the metallic orebodies and the Culm Group, respectively (Fig. 1).

MICROBIOLOGY OF THE RÍO TINTO SURFACE AND SUBSURFACE

Molecular and microbial ecology studies have shown that ca. 80% of the diversity in the surface environment comprises three bacterial genera that contribute to iron oxidation: *Acidithiobacillus*, *Leptospirillum* and *Acidiphilium* (González-Toril et al. 2003). Some species, such as *At. ferrooxidans,* oxidize ferrous iron aerobically and reduce ferric iron under anaerobic conditions (Malki et al. 2006; Ohmura et al. 2002), while *Leptospirillum* are aerobic iron oxidizers. Furthermore, *Acidiphilium* has been associated with the formation of siderite by oxidizing organic compounds using ferric iron as an electron acceptor (Fernández-Remolar et al. 2012). *Acidiphilium* can use ferric iron as an electron acceptor in the presence or absence of oxygen (Coupland and Johnson 2008; Malki et al. 2008). In addition, other iron-oxidizing bacteria (i.e., *Ferrovum* spp., *Ferrimicrobium* spp., *Ferroplasma* spp. and *Thermoplasma acidophilum*) or iron-reducing bacteria (i.e., *Ferrimicrobium* spp., *Acidisphaera* spp., *Metallibacterium* spp. and *Acidobacterium* spp.) have been identified in low numbers in the Rio Tinto basin (García-Moyano et al. 2012; González-Toril et al. 2003).

Regarding sulfur cycling, only *At. ferrooxidans* can aerobically and anaerobically oxidize both ferrous iron and sulfur. Sulfate-reducing microorganisms that complete the sulfur cycle have been detected in anaerobic areas of the river (García-Moyano et al. 2012; Sánchez-Andrea et al. 2011). In this regard, a comparative analysis of the sediments and the water column of different samples along the Río Tinto river (García-Moyano et al. 2012) has shown much higher levels of biodiversity in the anaerobic sediments than in the corresponding water column. Almost all the identified microorganisms were related to the iron cycle. While the majority of forms have been previously detected and/or isolated (see Amils and Fernandez-Remolar 2014, and references therein), some bacteria, such as members of *Actinobacteria*, *Firmicutes*, *Acidobacteria*, *Planctomycetes* and *Chloroflexi* phyla, have been recently discovered in the Río Tinto basin (García-Moyano et al. 2012). An interesting observation from the study of the anaerobic sediments of Río Tinto highlights that under strict anoxic conditions at the sediment bottom, sulfate reduction is a recurrent microbial activity that results from the high concentration of sulfates existing in the system.

Although the Río Tinto environment could be considered a harmful environment for eukaryotic life, it contributes over 60% of the Río Tinto basin biomass (Amaral-Zettler et al. 2002). However, while a great number of eukaryotic species are photosynthetic, fungi are a diverse group of organisms that can play a role in the subsurface of Río Tinto (Oggerin et al. 2013). In this regard, López-Archilla et al. (2005) identified more than 350 fungal isolates, revealing Ascomycetes as the most abundant phylum, while *Basidiomycetes* and *Zygomycetes* accounted for less than 2% of the sequenced isolates.

By using microbiological and molecular techniques on core samples, different bacterial and archaeal forms have been detected at different depths in the subsurface. These techniques included enrichment cultures, 16S rRNA cloning and sequencing, Fluorescence In Situ Hybridization and Catalized Reporter Deposition (CARD-FISH), and the LDChip200 and LDChip300 microsensors (Parro et al. 2008; Puente-Sánchez et al. 2014). The molecular and microbial analyses of the cores suggest that a

great portion of the microbial communities in the subsurface are composed of the same microbial forms that are found in the river environment (Amils and Fernández-Remolar 2014). Therefore, the S and Fe compounds in the subsurface are exposed to the same biogeochemical cycles that are ongoing at the surface of the Río Tinto river. As a result, different chemolithoautotrophs were detected, including aerobic and anaerobic pyrite oxidizers, which include anaerobic thiosulfate oxidizers that use nitrate as the electron acceptor as well as sulfate reducers (SRB) and methanogenic Euryarchaeota. Downstream of the metallic orebodies, dissolved sulfate in groundwater was in much higher concentrations that result from the interaction with the pyrite bodies. In this case, microbiological and molecular techniques have shown that sulfate-reducing and methanogenic activity were the main microbial processes occurring along the downstream section of the Rio-Tinto Variscan basement. Although dissolved H_2 was lower in BH1 than in BH4 and BH8 (Fernández-Remolar et al. 2008), there was enough to make it available as a microbial electron donor and release methane in concentrations that were several orders of magnitude higher than in BH4 and BH8.

METHODS

The geobiological study of the Río Tinto Variscan basement involved a multidisciplinary approach, including a survey of the surface and subsurface (hydro)geology. It was followed by mineralogical, geochemical and microbiological analysis of samples collected in the subsurface (Amils et al. 2013; Fernández-Remolar et al. 2008). The basement was inspected by geophysical soundings up to a depth of ca. 600 m in order to recognize the subsurface framework of the aquifers and metallic orebodies (Gomez-Ortiz et al. 2014; Jernsletten 2005), which are the essential components controlling the distribution of microbial communities underground. Such information was essential to select the location of the boreholes that sampled the microbial habitats of the Río Tinto basement. As discussed in the geological setting, the samples come from four boreholes, BH4, BH8, BH10 and BH11 (Fig. 1), performed by the MARTE and IPBSL projects that were developed to provide evidence of

underground microbial activity in the Río Tinto basement in Peña de Hierro (Amils et al. 2012; Fernández-Remolar et al. 2008).

Boreholes were continuously cored by rotary diamond-bit drilling using a Boart-Longyear HQ wireline system with 60 mm diameter cores. The coolant drilling fluid was well water that was re-circulated to lubricate the perforation bit. Sodium bromide (200 ppm) was added to the drilling fluid as a marker to detect potential contamination in samples. Upon retrieval from the drilling rig, cores were divided into 60 cm length parts, inspected for signs of alteration and stored in boxes for permanent storage and curation in the Instituto Geológico Minero de España (IGME) lithoteque in Peñaroya. Selected cores were deposited in plastic bags, oxygen was displaced with N_2, and the bags were sealed and transported to a field laboratory within 60 minutes. After drilling, boreholes were cased with PVC tubes with holes at different depths to allow water movement. Upon arrival at the field laboratory, cores were placed in an anaerobic chamber (5% H_2, 95% N_2), logged and photographed. Aseptic subsamples were obtained by splitting cores with a hydraulic core splitter and drilling out the central untouched portion with a rotary hammer with sterile bits and strict temperature control (40°C maximum). Rock leachates were produced by adding 5 ml sterile water to 0.5 g of powdered core subsamples and allowing them to stand overnight before filtration through pre-rinsed 0.2 μm nylon filters and analyzed in an Advanced Compact Ion Chromatographer (Metrohm AG). Small fragments of subsurface samples were coated with gold, paladium or osmium for SEM investigation, in order to recover microscopic and microanalytical information regarding the morphology and composition of the mineral and microbial structures found in the subsurface. Scanning electron microscopy and microanalysis was performed using Jeol JSM-5600 LV equipment coupled to a Cambridge INCAx-sight EDS (Electron Dispersive Spectrometer). SEM data analyses were obtained under beam conditions ranging from 10 to 20 keV accelerating voltage, which provided secondary and BSE images plus EDS/EDAX data that were analyzed using INCA Suite software. Therefore, the samples were prepared in a manner that would only allow for biomineralized structures to be targeted.

254

255

256

257 **RESULTS**

258

259 **Carbon-rich mineralized microstructures**

260 The coupled SEM-EDAX analysis of the borehole samples (Figs. 1-4) is a source of evidence that,
261 when combined with molecular and microbial techniques (Parro et al. 2008; Puente-Sánchez et al.
262 2014), supports the presence of microbial activity in the Río Tinto basement. The observation of
263 microbial structures in the subsurface samples suggests that there is a link between their morphology
264 and size and their depth and mineralogy. The biggest carbon-bearing microstructures consist of 10-15
265 μm well defined disc-like structures that are formed by the combination of two curved bacilli-like
266 structures attached to quartz (Fig. 2a) that are in close association with micrometer-sized, acicular Fe-
267 rich sulfates. Such discoidal structures laterally change to form clusters of smaller ovoidal and
268 elongated units (< 10 μm length) (Fig. 2a) occurring at a shallow depth (41 m). In the same depth
269 range, 3.5 to 4 μm oval cells (Fig. 2b) are also found on quartz. In this regard, Fernández-Remolar et
270 al. (2008) report the presence of some large microbial structures, such as filaments, mineralized at 21
271 m depth that have been characterized as fungal hyphae.

272

273 In areas deeper than 100 m, the microbial structures are usually much smaller (<1 μm) and appear in
274 close association with sulfur-bearing minerals. In this regard, there are three main morphologies
275 which include coccus-like, filamentous networks and upright filaments. At 134.5 m depth, colonies of
276 tiny (< 1 μm), disperse, spheroidal bodies (Fig. 2c) occur on pyrite surfaces where nanoscale cavities
277 with circular morphology also occur. The same microbial structures have been reported at a depth of

278 162 m by Fernández-Remolar et al. (2008) growing on similar pyrite surfaces and showing
279 mucilaginous capsule-embedding spheroid rows (Supp. Fig. 1) in BH8. Very distinctive structures
280 formed by intricate and dense networks of sinuous and overlapping filaments of few tens of
281 micrometers of lenght have been found at different depths below 100 m (Fig. 2d-e). They usually
282 emerge from the interior of 10 to 100 µm-sized pyrite cavities with straight boundaries (Fig. 2d).
283 Furthermore, the SEM analysis has revealed the presence of compact and dense colonies of 0.5 to 1
284 µm-sized angular-shaped mineralized structures (Fig. 3a) growing on a pyrite surface found at 157.5
285 m depth. Although such mineralized structures spread uniformly on the mineral surface (Rodríguez-
286 Navarro et al. 2012), they occasionally form linear clusters with signs of mineralization to carbonates
287 (Fig. 3a, Supp. Fig. 2). Such structures eventually show mucilaginous capsule-embedding (Supp. Fig.
288 3) as observed in the spheroid rows.

289

290 Very distinctive carbonaceous structures were observed in SEM in sample BH4. These structures
291 consisted of 3 to 5 µm-long upright filaments above the mineral surface with very thin diameter (ca.
292 100 nm) that uniformly cover the mineral surface of barite with a separation of 0.3 to 2 µm (Fig. 3b-e)
293 between two consecutive filaments. The exposure of the filaments to the SEM electron beam has
294 caused a partial or total obliteration of the microstructures, resulting in elongated to equidimensional
295 carbon-rich bodies less than 2 µm in length (Fig. 3b, d, e). In the extreme case of total obliteration of
296 filaments, they occur as a dotted, carbonaceous pattern on the mineral surface (Fig. 3c).

297

298 In some circumstances, the structures show mineralization, likely to siderite (Fernández-Remolar et
299 al., 2012), as some isolated clusters of straight and bent filaments that are present on barite surface
300 depressions (Fig. 3c, d; Supp. Fig. 4). Furthermore, this is also the case with the linear clusters of
301 ovoidal bodies mineralized, likely to Fe-carbonate, in sample 4-67a (157.5 m). The elemental
302 composition obtained through EDAX (Fig. 4a and 4b) has shown major elemental peaks for C, Fe, S
303 and O (Fig. 4a) that support the mineralization to iron carbonate as observed in other similar

304 structures (Supp. Fig. 2), but also with the presence of S-bearing compounds like elemental sulfur or
305 pyrite resulting from reduction of sulfate in barite. On the other hand, the surface is composed of
306 barite, as evidenced by major peaks of S, O and Ba (Fig. 4b). Interestingly, the barite surface is
307 densely covered by a dotted pattern of carbonaceous remnants that come from the obliteration of the
308 upright filaments under exposure of the SEM beam, which is supported by a high concentration of
309 carbon of ~ 42 in atomic percentage (Fig. 4b). The occurrence of carbon-rich organic matter
310 attenuates the fluorescent X-rays, with a greater attenuation for the lower-energy O and S X-rays than
311 for Ba (Goldstein et al. 2003), which increases the uncertainty in the (semi)quantification.

312

313

314 **Sulfur and iron minerals**

315 The samples collected at the uppermost part of the Río Tinto Variscan basement show an enrichment
316 in iron oxides and iron sulfates that result from complete oxidation of the orebody under aerobic
317 conditions. Iron oxyhydroxides (hematite and goethite) are very abundant in association with quartz
318 where microbial attack by chemolithotrophic aerobic communities has taken place (Sand et al., 2001).
319 Hematite and goethite have been identified by SEM-EDAX in the upper part of borehole BH4, in
320 samples 4-9a and 4-16a, collected at a depth of 19 and 32 m, respectively (Fig. 5), occurring as
321 colomorph intergrowths infilling the quartz crosscutting veins of hydrothermal origin (Fernández-
322 Remolar et al. 2008).

323

324 In those subsurface areas where the microbial oxidation is ongoing, there is a close association
325 between pyrite and ferric sulfates. Such minerals were found by SEM-EDAX in BH4, BH10 and
326 BH11 at different depths (Fig. 6) occurring as isolated rosettes, amorphous patches or mineral
327 coatings on pyrite. Interestingly, the mineral habit and size is related to the location where the acidic
328 sulfates precipitate with regard to the subsurface water level. Amorphous Fe-sulfate coatings and

329 rosettes (Fig. 6a-c) have been found below the water table, while large euhedral crystals usually occur
330 above the region under permanent saturation with subsurface solutions (Figs. 6d). In addition, there is
331 a close association between amorphous and rosette Fe-sulfate crystals and the occurrence of evidence
332 of microbial attack. There seems to be different stages of microbial attack, shown first as simple
333 circular and elongate nanoscale pits, arrays of pits and linear scars (Fig. 6b). They evolve to fully
334 corroded surfaces with deep cavities that are filled with carbon-rich materials (Fig. 6a; Supp. Fig. 5).
335 Furthermore, crystals of primary barite have been found with clear signs of corrosion in BH4 (Fig. 7a)
336 at a depth of 77 m, which is a few meters above the water level. Although barite of hydrothermal
337 origin (~345 Ma) is associated with primary quartz and phyllosilicates as well (Leistel et al., 1998), it
338 co-occurs with secondary iron oxyhydroxides that coat the corrosion scars formed in the barite crystal
339 (Fig. 7a).

340

341 In deeper areas, the SEM images show that barite crystals have been exposed to different degrees of
342 chemical dissolution (Figs. 7b and 8). In BH4, at a depth of 126 m, the microscopy analysis of sample
343 4-50b reveals a prismatic barite crystal with a local attack on areas of the crystal surface followed by
344 precipitation of complex Fe-carbonate spheroids (Fig. 7c). Such a process develops in deeper areas, as
345 shown in samples 8-67a and 8-68c (Fig. 8) that were collected at 157.5 and 163 m, respectively. In
346 sample 8-67a, the barite surface shows an extensively weathered surface with a dotted pattern (Fig.
347 8a). The barite surface is coated with a carbonate lamina of approximately 2 μm in thickness (Fig.
348 8a1) consisting of tightly packed filamentous tabular crystals. Although the siderite lamina coats the
349 barite surface, this occurs above an empty interval of less than 1 μm of thickness (Fig. 8a). In other
350 cases, the degree of barite corrosion is greater and occurs as isolated fragments of crystals embedded
351 in a mass of 25 μm in size, intergrowing carbonates with filamentous microstructure (Fig. 8b).

352

353 The SEM-EDAX study of the subsurface samples has also revealed a close association between
354 siderite, pyrite and quartz in underground areas below the water table. In this regard, pyrite crystals

355 co-occur with siderite spheroids and disc-shaped laminas (Fig. 9a, b, c) that contact the sulfide surface
356 through irregular boundaries and infilling of some cavities. The siderite spheroids can occur in the
357 form of complex aggregates with rosettes fully embedding the pyrite crystals (Fig. 9a). However,
358 some spheroid aggregates can show amorphous microstructure without any evidence of filamentous
359 microstructure. Occasionally, some spheroids seem to fill preexistent cavities that have internal planar
360 sides (Fig. 9c). Interestingly, the siderite frequently shows a disc-shaped appearance when covering
361 silica-rich primary minerals like chlorite (Fig. 9d) and quartz (Fernández-Remolar et al. 2008).

362

363 DISCUSSION

364 **Microbial structures**

365 The morphology, size and/or composition of some microstructures and its association with different
366 mineral surfaces suggests that correspond to microbial remains. They show different degree of
367 biomineralization ranging from carbonaceous to mineralized carbonatic morphologies. In the first
368 group of carbonaceous microstructures, a very diverse morphologies are found that comprise the
369 curved bacilli-like structures attached to quartz (Fig. 2a) which laterally change to form clusters of
370 smaller ovoidal and elongated units (< 10 μm length). Furthermore, the co-occurrence of disperse,
371 spheroidal bodies (Fig. 2c) and nanoscale cavities with circular morphology on pyrite surfaces show
372 evidence of bacterial cocci that are attacking the sulfide surface. This is also observed in the
373 carbonaceous rich structures represented by frameworks of sinuous and overlapped filaments (Fig. 2d-
374 e), which resemble bacteria exopolysaccharide (EPS) and filamentous structures described by Urwins
375 et al. (1998). They usually emerge from the interior of 10 to 100 μm-sized pyrite cavities with straight
376 boundaries (Fig. 2d) that suggest an intensive microbial attack along crystallographic planes or
377 structural weakness through the oxidation of sulfide (Welch and Vandevivere, 1994; Zhou et al.
378 2011). In addition, the occurrence of upright carbonaceous filaments that uniformly cover barite
379 surfaces (Fig. 3b-e) suggests that they might be filamentous bacteria, which obtain energy through
380 metabolizing sulfate ions. In this regard, the occurrence of corroded surfaces with deep cavities that

are filled with carbon-rich compounds (Fig. 6a; Supp. Fig. 5) suggests that the microbial attack on pyrite is also an oxidative process which has been recorded as ferric sulfates.

A second group of strucures that are associated to microbial morphologies show mineralization to Fe-carbonates. This is the case of ovoidal microstructures resembling coccus bacterial morphologies that sometimes occur as linear clusters (Figs. 3a; Supp. Figs. 2 and 3) of ovoid-like units, which are mineralized to Fe-carbonate as shown in EDS spectra. Similar microstructures with linear arrangement (Fig. 4) could correspond to the mineralization to carbonate of primary filamentous microbes. In addition, other structures of bigger size, while cannot be considered as the mineralization of microbial cells, they could be the result of the microbial metabolism of SRB. They correspond to complex Fe-carbonate spheroids (Figs. 7c, 8b and 9a-d) that infill voids formed in the mineral surfaces which formation is discussed below.

Biogeochemical processes

The distribution of iron and sulfur compounds provides essential information with regard to the biogeochemical processes that have been operating over the most recent millions of years in the Río Tinto subsurface (Essalhi et al. 2011; Fernández-Remolar et al. 2008). Such activity has been recorded in the surface as different gossan and terrace levels that are mainly composed of iron oxyhydroxides with trace levels of sulfates (Fernández-Remolar et al. 2005). The SEM-EDAX analysis of the samples occurring in shallower areas of the Río Tinto Variscan basement supports that the main process was led by oxidative and acidic conditions. This is the paradigmatic case of the enrichment in iron oxyhydroxides (Figs. 1 and 5) at the vadose area of the subsurface. However, oxyhydroxide formation took place during mineral maturation of the secondary acidic sulfates (Fernandez-Remolar et al. 2011), which originated from a complex, direct and indirect microbial attack to the pyrite (Sand et al. 2001) as shown in the following reactions:

406

407 $FeS_2 + H_2O + 3.5\ O_2 \rightarrow Fe^{2+} + 2\ SO_4^{2-} + 2\ H^+$

408 $Fe^{2+} + ¼\ O_2 + H^+ \rightarrow Fe^{3+} + ½\ H_2O$

409 $FeS_2 + 14\ Fe^{3+} + 8\ H_2O \rightarrow 15\ Fe^{2+} + 2\ SO_4^{2-} + 16\ H^+$

410

411 As a result, the biooxidation process acidifies the incoming meteoric solutions (pH 5.5 to 6) that are
412 oversaturated with SO_4^{2-} and Fe^{3+} that have been interacting with the sulfide orebodie along the last 25
413 Ma (Essalhi et al. 2011). Under the surface and subsurface oxic areas of Río Tinto, the main minerals
414 that precipitate are jarosite and schwertmannite (Fernández-Remolar et al. 2005). Under these
415 conditions, the formation of iron oxyhydroxides in the gossan upper unit and terraces is the result of a
416 complex diagenesis of the acidic sulfates that combines mineral dehydration and exposure to mild
417 acidic meteoric waters. Consequently, the final mineral phases are the iron oxyhydroxides that are
418 favored under a pH ranging from mildly acidic to alkaline. Assuming that schwertmannite is the main
419 mineral phase that precipitates out from the acidic solutions (Burton et al., 2008; Peretyazhko et al,
420 2009), the following reaction expresses the maturation process of the acidic product to iron
421 oxyhydroxides:

422

423 $Fe_8O_8(OH)_{5.5}(SO_4)_{1.25} + 2.5\ H_2O \rightarrow 1.25\ SO_4^{2-} + 8\ FeOOH + 2.5\ H^+$

424

425 Therefore, the occurrence of the iron oxyhydroxides at the top of the iron sulfides is a relic of the
426 ancient microbial activity when the aquifer water table was in shallower areas of the basement which
427 contains sulfides in form of massive orebodies or disseminated pyrite from surface areas up hundreds
428 of meters deep (Gómez-Ortiz et al. 2014). After migrating downwards by different geological
429 processes, the acidic sulfates were precipitated and exposed to a combined process of dehydration and

ion transportation by meteoric solutions (Fernandez-Remolar et al. 2005). Such a mechanism is the same as for the formation of the iron-rich terraces. These were sedimentary bodies originally formed by ferric sulfates that, after being exposed to meteoric waters as a consequence of the river entrenchment, evolved to deposits composed of iron oxyhydroxides.

The association of microbial bodies with iron oxyhydroxides with a size of 15 to 3.5 micro-meters (Fig. 2a, b) supports the existence of eukaryotic and bacterial aerobic activity, which promotes acifdification under the oxidation of iron sulfides. This is also consistent with the detection of crystalline ferric sulfates (Figs. 2a and 6c) that is the result of precipitation from acidic solutions above the water table. Interestingly, both ferric sulfate structures, including star-like clusters of fibers (Fig. 2a) and rhomboids (Fig. 6c), are formed on quartz mineral surfaces. This finding suggests that dissolved ferric sulfates precipitated from migrating fluids along the vadose area due to supersaturation, where microbial activity played an indirect role. Furthermore, the formation of the ferric sulfates could also be related to the maturation processes leading to oxyhydroxide compounds. Such processes include the release of SO_4^{2-} and different cations that are mobilized by meteoric waters following a seasonal input (Fernández-Remolar et al. 2003; Gómez-Ortiz et al., 2014). The chemical conditions of the solutions that were acting in the oxic region of the basement have been recorded in the form of dissolution surfaces affecting minerals with low solubility constants, such as barite (Fig. 7a). In sample 4-32a, collected above the water table at 77 m (Fig. 1), barite and quartz crystals have been exposed to a planar dissolution that is followed by the massive formation of iron oxyhydroxides on the dissolution surface. Whether or not acidic sulfates could be a phase transition to iron oxyhydroxides, the dissolution of barite and quartz requires strongly acidic solutions which would be followed by the precipitation of iron-bearing minerals. Barite dissolution is favored by low pH solutions as follows:

$$BaSO_4 + H_3O^+ \rightarrow HSO_4^- + Ba^{2+} + H_2O$$

456

457 Under such acidic and oxic conditions found in the Río Tinto Variscan basement, the optimal
458 dissolution of barite would have occurred at an acidic pH. In this regard, the dissolution of quartz
459 along the same dissolution front, as suggested by the occurrence of iron oxyhydroxides following the
460 same surface that is dissecting the quartz and barite crystals (Fig. 7a), should result of a very
461 aggressive dissolution occurring under a pH ranging between 0 and 2.5 and an high temperature (90-
462 100 °C) that can be reached during the oxic oxidation of the massive sulfides in the subsurface
463 (Crundwell, 2014; Leybourne et al. 2009).

464

465 Below the water table, there is clear evidence of microbial attack on the pyrite surfaces that come
466 together with rosettes and amorphous patches of iron sulfates (Fig. 6a-c). The co-occurrence of the
467 carbon-rich compounds inside the corrosion cavities with patchy Ferric sulfides and microbial fabrics
468 (e.g., pits, linear to sinuous corrosion) on the pyrite surface strongly suggests an extensive microbial
469 attack that is the source of the acidic conditions observed in BH11 ($pH < 3.5$, $Eh > 450$ mV). This
470 corrosion process could also have been driven by abiotic mechanisms discussed by Edwards et al.
471 (1999). However, under acidic conditions, where oxygen is inhibited as an oxidation agent, the pyrite
472 corrosion is driven by the combination of direct and indirect oxidation mechanisms that are triggered
473 by microbial activity (Sand et al. 2001). Consequently, the main biogeochemical processes occurring
474 in the upper acidic and oxic region of the Río Tinto Variscan basement correspond to the precipitation
475 and/or remobilization of sulfate minerals in the vadose area and pyrite biooxidation. Both processes
476 release sulfate and ferric iron to deeper regions that can eventually be used as electron acceptors in
477 different metabolic pathways that involve pyrite oxidation by ferric iron and sulfur reduction
478 (Fernández-Remolar et al., 2008).

479

480 In deeper regions of the Río Tinto subsurface, the association of barite euhedral crystals with
481 spheroidal to laminar siderite with filamentous fabric and microbial structures (Figs. 7c and 8)

strongly suggests that siderite is the final component of a process started by the microbial attack on the barite surface. Regardless of whether the sulfate reduction is a common process in the anaerobic regions of terrestrial crust, as in the Río Tinto subsurface (Fernández-Remolar et al. 2008), little has been reported concerning barite as a potential electron acceptor. In this respect, Bolze et al. (1974) describe the microbial mobilization of barite when sulfur-reducing bacteria are grown with powdered minerals under anaerobic conditions. The occurrence of upright filaments (Supp. Fig. 6) that have been obliterated during the EDS analysis to bacterial remnants by the electron beam (Fig. 3c-e) suggests that SRB are currently mobilizing barite in the anaerobic regions of the Río Tinto subsurface. This is supported by the occurrence of such filaments that are growing upright on the barite surface and which are filling the empty interval separating both siderite and barite as shown in Fig. 8a. Consequently, the sulfate reducers promote the generation of S mobilization fronts in barite that approach a spherical morphology (Fig. 7b). However, sulfur mobilization recorded in the form of siderite with a microbial-like microstructure (Figs. 3c-d, 4c, and 7a) suggests that some additional microbial process involves carbonate biomineralization. This could be the result of the oxidation of the organic compounds produced by the SRB that could be metabolized by chemoheterotrophic microbes, such as *Acidiphilium* sp. and *Tessarococcus lapidicaptus,* and promoting the precipitation of siderite under anaerobic conditions. Both microbes have been reported to produce siderite in the anaerobic areas of Río Tinto, including the basement (Fernández-Remolar et al. 2012; Sánchez-Roman et al. 2014, 2015). However, the formation of carbonate following iron reduction requires continuous support of ferric iron, which is highly available in the surface environment of Río Tinto but not in the subsurface. While ferric iron could be supplied from the surface by the mobilization by oxic waters through faults, carbonate could be produced directly from the activity of SRB (Castanier et al. 1999; Baumgartner et al. 2006). Therefore, carbonate could be produced by SRB respiration, in which an organic substrate is metabolized, after pH increase by local concentration of HCO_3^- at the microscale (Baumgartner et al 2006):

$$SO_4^{2-} + 2\ (CH_2O)\ \text{(organic matter)} + Fe^{2+} \rightarrow FeCO_3 + CO_2 + H_2S + H_2O$$

509

510 Where pyrite could be secondarily formed under the following process (Drobner et al. 1990;
511 Fernández-Remolar et at. 2008):

512

513 $2\ H_2S + Fe^{2+} + 1/2\ O_2 \rightarrow FeS_2 + 2\ H^+ + H_2O$

514

515 Interestingly, the microbial reduction of sulfate in barite could also be mediated by using methane as a
516 substrate (Zhu and Dittrich 2016). As methane has been reported in the Río Tinto Variscan basement
517 (10-95 ppm in subsurface waters, Fernández-Remolar et al. 2008), it could be an additional source of
518 energy used by SRB in the following reaction:

519

520 $CH_4 + BaSO_4 + Fe^{2+} \rightarrow FeCO_3 + H_2S + Ba^{2+} + H_2O$

521

522 In both cases, the formation of the siderite laminar and spheroidal structures (Supp. Fig. 7) can be
523 explained as the growth of the microbial colony into the barite crystal by facilitating the precipitation
524 of ferrous carbonates (Fernández-Remolar et al. 2012; Sánchez-Roman et al. 2014). Carbonate growth
525 would proceed through sulfate mobilization and reduction along the dissolution fronts driven by the
526 microbial dynamics (Supp. Fig. 7). As the mobilization process is proceeding, siderite mineralization
527 would occur in the external part of the colony where HCO_3^- anions would migrate and concentrate
528 along a pH gradient (Fig. 10) which is increased towards the microsites where bicarbonate is
529 produced through the microbial oxidation of organics (Fernández-Remolar et al., 2012). Such a pH
530 gradient occurring at microscale would be created by the overconcentration of organic acids that are
531 used by bacteria to mobilize ions from mineral surfaces (Bebié and Schoonen 2000).

532

Interestingly, the collection of rocky samples in deep areas of the Río Tinto subsurface have provided some evidence of mineral microbial corrosion. This is the case for the occurrence of microbial structures co-occurring with microfabrics ranging from nanoscale corrosion traces to microcavities of tens of microns (Welch and Vandevivere, 1994; Zhou et al. 2011) occupied by biomineralized microbial structures (Figs. 2c-e and 4a-b) found in anoxic regions of the subsurface below 115 m depth. They occur in three different settings as follows: 1) nanoscale pits associated with coccus-like microbial bodies (Fig. 2c); 2) tens of microns-sized elongated pyrite cavities with straight boundaries occupied or associated with dense networks of filamentous C-rich structures of EPS (Fig. 2d-e); and 3) equidimensional cavities (< 5 μm) infilled with clusters of coccus-like microbial bodies (Fig. 4a-b) at greater depth (311.75 m).

The correlation between the microbial structures and the corrosion microfabrics affecting the pyrite surface suggests that the microbial communities utilize different approaches for corrosion. While the coccus-like microbes produce microfabrics on the mineral surface going from nanoscale pits to equidimensional cavities, the filamentous networks forming biofilms show an intensive microbial attack along crystallographic planes or structural weakness in the mineral. As there is no mineral by-product associated with the corrosion microfabrics, it is difficult to determine the metabolic process involved in pyrite degradation, if any. The corrosion process could correspond to pyrite oxidation under anaerobic conditions, which is mediated by the indirect biooxidation of sulfide (Sand et al. 2002). This agrees with the occurrence of Fe^{3+} and SO_4^{2-} (Fig. 1) (Fernández-Remolar et al. 2008), which show average concentrations of 4 and 2.5 mM, respectively, in the subsurface solutions from areas deeper than 110 m from BH4, BH8 and BH10. Therefore, it is very likely that under anaerobic conditions, the formation of ferric sulfates are inhibited, and ferric sulfates would not form as has been observed in the oxic areas of the aquifer where the microbial corrosion microfabrics are associated with ferric sulfate patches (Fig. 6a-c).

As indirect microbial oxidation of pyrite produces 14 moles of H^+ for each mole of pyrite (Sand et al. 2002), the subsurface solutions should become extremely acidic. However, this is not the case because where the corrosion microfabrics occur, the pH of solutions is neutral. The absence of acid fluids could be related to the production of hydrogen that has been detected in the anoxic regions of the Río Tinto basement (Fernández-Remolar et al. 2008). The production of hydrogen could be directly linked to pyrite attack by protons that have been previously released through the indirect biooxidation of pyrite. This could occur as a secondary biogeochemical pathway expressed with the following reaction (Rickard and Luther, 2007):

$$FeS_2 + H^+ \rightarrow S^{2-} + Fe^{3+} + \tfrac{1}{2} H_2$$

where the protons would be released by anaerobic biooxidation.

Furthermore, the continuous supply of ferric iron to the anaerobic area of the basement could also be from the migration of shallow solutions through faults. Such a process would be greatly accelerated during the wet season (Fernández-Remolar et al. 2003) that supplies meteoric waters enriched with oxidized compounds from the vadose area. This agrees with the occurrence of fractures and faults in the locations where the sulfate and ferric iron concentrations are increased (Fig. 1).

In this context, the co-occurrence of spheroidal siderite with pyrite that shows clear signs of corrosion (Fig. 9a, d) could be a consequence of organic oxidation using SO_4^{2-} as the electron acceptor. In this case, the anaerobic formation of siderite would come from the release of Fe^{2+} through the pyrite oxidation or degradation. As has been reported for chemoheterotrophic bacteria like *Acidiphillium sp.* occurring in the river (Fernández-Remolar et al., 2012; Sánchez-Roman et al. 2015), Fe-carbonates

583 can form by the oxidation of organic matter using Fe^{3+} as electron acceptor. In this regard, siderite
584 precipitate could be directly formed through the heterotrophic release of HCO_3^- when organic
585 compounds are available. While siderite formation could be formed in the aerobic Río Tinto solutions
586 that show an average Fe^{3+} concentration of ~ 15 mM, it could also be precipitated in the subsurface
587 through the release of ferrous iron by microbial oxidation of pyrite. This could be the case for the
588 presence of disc-like siderite structures on silicic minerals, such as quartz and chlorite (Fig. 9b-c),
589 which come together with phosphate-bearing compounds, as described by Fernández-Remolar et al.
590 (2008).

591

592 Both processes, including the sulfate reduction from barite and the pyrite anaerobic oxidation, require
593 ion mobilization from the mineral surfaces to be available for microbial metabolism. Although there
594 are different mechanisms used by the microbes (Bebié and Schoonen 2000), the high concentration of
595 organic acids like oxalates (> 2 ppm) at some depths of the basement unaffected by faulting suggest
596 that organic acids are used to mobilize ionic substrates (e.g., SO_4^{2-}) to sustain chemolithotrophic
597 metabolism. In this context, the overconcentration of organic acids that have been derived from the
598 interaction between microbes and the lithosphere would be a complementary set of biosignatures of
599 cryptic life for any planetary body.

600

601 IMPLICATIONS

602 The two main hydrothermal scenarios for the possible origin of life on Earth, that of vents on the
603 ocean floor and that of volcanic fields at the surface, are also found on Mars (Deamer and Damer,
604 2017, Michalksi et al. 2017; Sholes et al. 2017). Under these circumstances, the geochemical
605 processes occurring in the hydrothermal systems of early Mars under a higher concentration of Fe and
606 S (Barlow, 2008; King and McLennan 2010) very likely favored the emergence of chemical cycles
607 mimicking some biochemical pathways found in chemoauthotrophic organisms (Wächtershäuser
608 1992). Therefore, the possible existence on Mars of a mineral sulfur/iron-energy deriving Earth-like

609 microbial life would have even been more probable than on Earth. Thus, the oxidative formation of
610 pyrite (FeS_2) from hydrogen sulfide volatiles (HS^-, H_2S) interacting with FeS (e.g. pyrrothite) provide
611 a simple chemical route to transfer electrons by the so-called pyrite-pulled reaction (Wächtershäuser
612 1992) following the geochemical pathway:

613

614 $FeS + H_2S \rightarrow FeS_2 + H_2$

615

616 They would have easily operated in the Mars crust given its redox state, which has been estimated
617 between ~1 log unit below FMQ (Fayalite-Magnetite-Quartz) and ~ 1 log unit below IW (Iron-
618 Wustite) (Sholes et al. 2017; Wadhwa 2008). QFM and IW correspond to mineral buffers of the
619 interior of planetary bodies that partly control the composition of the volatiles released to the
620 atmosphere (Ehlmann et al. 2016). These geochemical processes are more exergonic at pH below 6.5
621 and at an increasing temperature, which match with an acidic and thermophilic origin of life as
622 discussed by Wächtershäuser (1992). Given the geochemical conditions of early Mars, the electron
623 transfer mediated by S and Fe bearing compounds in the Mars crust could have certainly operated to
624 provide the enough chemical energy to sustain an early metabolism. In this regard, the pyrite-pulled
625 reaction would have played an essential role in the fixation of carbon. It would occur by the reduction
626 of CO_2 that is a common volatile in different hydrothermal settings The CO_2 reduction through the
627 mimic an incipient biochemical fixation of carbon (Wächtershäuser 1992, and references therein) in
628 form of carboxylate ($HCOO^-$) as prebiotic precursor, followed by the generation of more reduced C-
629 bearing compounds:

630

631 $HCO_3^- + FeS + H_2S \rightarrow HCOO^- + FeS_2 + H_2O$

632 $HCOO^- + FeS + H_2S + H^+ \rightarrow H_2CO + H_2O + FeS_2$

633

634 The emergence of a biogeochemical cycle could have started at the formation of carboxylate
635 (Wächtershäuser 1992) and completed by the fixation of formaldehyde that is a building block for
636 some essential biomolecules as sugars on early Earth (Cleaves 2008). This early biochemical cycle
637 could have equally emerged in hydrothermal centers on Mars (Deamer and Damer, 2017, Michalksi et
638 al. 2017), where redox state and geochemical composition enriched in S, Fe and C-bearing
639 compounds could have interplayed to form prebiotic precursors (Herschy et al 2015; Lane and Martin
640 2012). Indeed, some biogeochemical pathways involved in the formation of mineral biosignatures in
641 the Rio Tinto basement resemble or are reverse to biochemical processes emerging in a Fe and S
642 world (Wächterhäuser 1992). This is the case of the generation of HCO_3^- through the oxidation of
643 organic compounds, when SRB metabolize sulfate bearing minerals like barite. Interestingly, such
644 biogeochemical process is coupled to the formation of pyrite and hydrogen following the pyrite-pulled
645 reaction. Consequently, the activity of a putative biosphere in the Mars subsurface should have been
646 produced a mineral record comparable to the archive of secondary minerals produced by
647 chemotrophic microbial activity in the Rio Tinto subsurface.

648

649 The high concentration of sulfur and iron minerals in the crust of Mars suggests that they can sustain
650 microbial communities through biogeochemical cycles propelled by differences in the redox
651 conditions between the surface and subsurface (Fernández-Remolar et al. 2008). The extensive
652 distribution of sulfates in the Mars surface (Grotzinger and Milliken 2012, and references therein)
653 strongly supports that the planet had a reservoir with a sulfide-rich protolith that was later exposed to
654 strong oxidation in the Hesperian (McCubbin et al. 2009; Gaillard et al. 2013). Under these
655 conditions, microbial life could function through the biogeochemical cycling of sulfur and iron as a
656 result of the redox difference between the upper oxidized crust and the deeper anoxic regions of the
657 planet (Michalski et al. 2013). In this context, the structures and minerals described in this article
658 would highlight the conditions and microbial processes that can occur in the Mars underground. Mars

659 has experienced several hydrological cycles occurring in the early Noachian (Andrews-Hanna and
660 Lewis 2011), during the late Noachian and early Hesperian that produced the network valleys (Di
661 Achille and Hynek 2010), and in the late Hesperian to early Amazonian (Molina et al. 2017). During
662 these hydric episodes water was abundant enough to interact with the Martian crust. Under these
663 conditions, sulfate and other ions could have been easily mobilized and transported underground. In
664 addition, different sulfate bearing minerals sourced in the Mars hydrothermal activity, as well as by
665 diagenesis in sedimentary deposits (King and McLennan 2010; Vaniman et al. 2014) can provide the
666 chemical disequilibrium in the subsurface to sustain sulfur reducing microorganisms. Organic
667 compounds and different ions could provide the energy source that would promote the reduction of
668 sulfate in the subsurface. As discussed by Michalski et al. (2013), the main geochemical process
669 occurring in the deep Mars crust of the southern highlands may have produced CH_4 and H_2 through
670 serpentinization. As methane and other short chained organics can be formed under hydrothermal
671 conditions (Huber and Wächterhäuser 1997; Simoniet 2004), the underground biosphere of Mars
672 could have used the C-bearing compounds as electron donors to reduce the sulfate minerals in the
673 crust of Mars. In addition, the use of inorganic compounds (e.g. Fe^{2+}, H_2) as electron donors would
674 also sustain a subsurface biosphere under the reduction of sulfate-bearing minerals. Under strong
675 anoxic and alkaline conditions in the subsurface, down-welling acidic solutions enriched in sulfates
676 would have provided the chemical disequilibrium through a strong geochemical gradient depending
677 on pH and redox potential. This is, to some extent, the same configuration of the Río Tinto basement
678 that is seasonally supplied by acidic meteoric solutions. Therefore, the use of methane, hydrogen and
679 short-chain organic compounds derived from serpentinization (Wang et al 2014, and references
680 therein) could have acted as an energy source for sulfur and iron microbial cycling. Therefore, the
681 sulfate groups in minerals like gypsum, anhydrite, and basanite, which are abundant mineral phases
682 on Mars (Grotzinger and Miliken 2012; Nachon et al. 2014), could have acted as electron acceptors,
683 mimicking the same process observed in barite in the Río Tinto. Whether or not the organic
684 compounds would have been highly available to form carbonate-bearing biosignatures, the
685 atmospheric and/or geological supply of CO_2 in the Mars subsurface would have been enough to
686 promote carbonate formation. This would be favored under neutral to alkaline and anoxic conditions

687 which have been claimed for some potential underground habitats on Mars (Fernández-Remolar et al.
688 2008; Michalski et al. 2013). Furthermore, the existence of a cryptic biosphere fueled by mobilized
689 ionic compounds from the upper lithosphere should be associated with the production of organic acid
690 compounds that should concentrate in the Mars underground. Consequently, a high concentration of
691 such materials in the subsurface could provide clear signs of microbial life in the Mars crust.

692 The emergence of chemotrophic life metabolizing S and Fe inorganic compounds is consistent with
693 the early hydrothermal and volcanic activity, as well as the abundance of sulfur- and iron-bearing
694 minerals in the Mars crust. It suggests that the Río Tinto-type mineral biosignatures which are formed
695 through metabolizing S and Fe compounds in the subsurface can be useful in the search for extant and
696 extinct subsurface life on the red planet. Furthermore, potential traces of life formed in the Mars
697 underground would have greater chances to be preserved given they are protected against billions of
698 years of watery activity interplaying with strong oxidizing and radiation conditions. Consequently,
699 whether or not life raised on Mars, one first-class target to answer this essential question can be found
700 in the subsurface. In the underground, a stable biosphere sustained by the iron and sulfur geochemical
701 cycles could have risen and diversified. While in the planet surface, where conditions were changing
702 and extreme, the environmental conditions were challenging for life.

703

704 ACKNOWLEDGMENTS

705

706 This study was supported by the projects NRA-02-OSS-01 ASTEP Mars Astrobiology Research and
707 Technology Experiment (MARTE) and Iberian Pyrite Belt Subsurface Life IPBSL (funded by the
708 European Research Council) projects. Authors appreciate the strong support provided by the MARTE
709 and IPBSL Science and Technology Teams. Authors are grateful for the ideas provided by Prof.
710 Gordon Southam and Dr. Jeremiah Shuster, Dr Javier Cuadros, Dr Amy Williams and one anonymous
711 reviewer, who have greatly improved the manuscript.

712

713 REFERENCES CITED

714

715 Amils, R., and Fernández-Remolar, D.C. (2014) Río Tinto: A Geochemical and Mineralogical
716 Terrestrial Analogue of Mars. Life, 4, 511-534.

717 Amils, R., Fernández-Remolar, D.C., Parro, V., Rodríguez-Manfredi, J.A., Timmis, K., Oggerin, M.,
718 Sánchez-Román, M., López, F.J., Fernández, J.P., Puente, F., Gómez-Ortíz, D., Briones, C.,
719 Gómez, F., Omoregie, E., García, M., Rodríguez, N., and Sanz, J.L. (2013) Iberian Pyrite Belt
720 Subsurface Life (IPBSL), a drilling project of biohydrometallurgical interest. Advanced
721 Materials Research, 825, 15-18.

722 Andrews-Hanna, J.C., and Lewis, K.W. (2011) Early Mars hydrology: 2. Hydrological evolution in
723 the Noachian and Hesperian epochs. Journal of Geophysical Research: Planets, 116(E2),
724 10.1029/2010JE003709.

725 Banfield, J.F., Moreau, J.W., Chan, C.S., Welch, S.A., and Little, B. (2001) Mineralogical
726 Biosignatures and the Search for Life on Mars. Astrobiology, 1(4), 447-465.

727 Barlow, N.G. (2008) Mars: An Introduction to Its Interior, Surface, and Atmosphere. Cambridge
728 University Press.

729 Baumgartner, L.K., Reid, R.P., Dupraz, C., Decho, A.W., Buckley, D.H., Spear, J.R., Przekop, K.M.,
730 and Visscher, P.T. (2006) Sulfate reducing bacteria in microbial mats: Changing paradigms,
731 new discoveries. Sedimentary Geology, 185(3–4), 131-145.

732 Bebié, J., and Schoonen, M.A.A. (2000) Pyrite surface interaction with selected organic aqueous
733 species under anoxic conditions. Geochemical Transactions, 1(1), 47.

734 Bolze, C., Malone, P.G., and Smith, M.J. (1974) Microbial mobilization of barite. Chemical Geology,
735 13, 141-143.

736 Brocks, J.J., and Summons, R.E. (2003) Sedimentary hydrocarbons, biomarkers for early life. In W.H.
737 Schlesinger, Ed. Treatise in Geochemistry, 8, p. 64-115. Elsevier.

738 Burton, E.D., Bush, R.T., Sullivan, L.A., and Mitchell, D.R.G. (2008) Schwertmannite transformation
739 to goethite via the Fe(II) pathway: Reaction rates and implications for iron–sulfide formation.
740 Geochimica et Cosmochimica Acta, 72(18), 4551-4564.

741 Castanier, S., Le Métayer-Levrel, G., and Perthuisot, J.-P. (1999) Ca-carbonates precipitation and
742 limestone genesis — the microbiogeologist point of view. Sedimentary Geology, 126(1–4), 9-
743 23.

744 Huber, C., and Wächtershäuser, G. (1997) Activated Acetic Acid by Carbon Fixation on (Fe,Ni)S
745 Under Primordial Conditions. Science, 276(5310), 245.

746 Cleaves, H.J. (2008) The prebiotic geochemistry of formaldehyde. Precambrian Research, 164(3),
747 111-118.

748 Coupland, K., and Johnson, D.B. (2008) Evidence that the potential for dissimilatory ferric iron
749 reduction is widespread among acidophilic heterotrophic bacteria. FEMS Microbiology
750 Letters, 279, 30-35.

751 Crundwell, F.K. (2014) The mechanism of dissolution of minerals in acidic and alkaline solutions:
752 Part II Application of a new theory to silicates, aluminosilicates and quartz. Hydrometallurgy
753 149, 265-275.

754 Davis, R.A., Welty, A.T., Borrego, J., Morales, J.A., Pendon, J.G., and Ryan, J.G. (2000) Río Tinto
755 estuary (Spain): 5000 years of pollution. Environmental Geology, 39(10), 1107-1116.

756 Deamer, D., and Damer, B. (2017) Can Life Begin on Enceladus? A Perspective from Hydrothermal
757 Chemistry. Astrobiology, 17(9), 834-839.Di Achille, G., and Hynek, B.M. (2010) Ancient
758 ocean on Mars supported by global distribution of deltas and valleys. Nature Geosci, 3(7),
759 459-463.

760 Drobner, E., Huber, C., Wächtershäuser, G., Rose, D., and Stetter, K.O. (1990) Pyrite formation
761 linked with hydrogen evolution under anaerobic conditions. Nature, 346, 742-744.

762 Ehlmann, B.L., Anderson, F.S., Andrews-Hanna, J., Catling, D.C., Christensen, P.R., Cohen, B.A.,
763 Dressing, C.D., Edwards, C.S., Elkins-Tanton, L.T., Farley, K.A., Fassett, C.I., Fischer,
764 W.W., Fraeman, A.A., Golombek, M.P., Hamilton, V.E., Hayes, A.G., Herd, C.D.K., Horgan,
765 B., Hu, R., Jakosky, B.M., Johnson, J.R., Kasting, J.F., Kerber, L., Kinch, K.M., Kite, E.S.,
766 Knutson, H.A., Lunine, J.I., Mahaffy, P.R., Mangold, N., McCubbin, F.M., Mustard, J.F.,
767 Niles, P.B., Quantin-Nataf, C., Rice, M.S., Stack, K.M., Stevenson, D.J., Stewart, S.T.,
768 Toplis, M.J., Usui, T., Weiss, B.P., Werner, S.C., Wordsworth, R.D., Wray, J.J., Yingst, R.A.,
769 Yung, Y.L., and Zahnle, K.J. (2016) The sustainability of habitability on terrestrial planets:
770 Insights, questions, and needed measurements from Mars for understanding the evolution of
771 Earth-like worlds. Journal of Geophysical Research: Planets, 121(10), 1927-1961.

772 Essalhi, M., Sizaret, S., Barbanson, L., Chen, Y., Lagroix, F., Demory, F., Nieto, J., Sáez, R., and
773 Capitán, M.Á. (2011) A case study of the internal structures of gossans and weathering
774 processes in the Iberian Pyrite Belt using magnetic fabrics and paleomagnetic dating.
775 Mineralium Deposita, 46(8), 981-999.

776 Fernández-Remolar, D.C., Morris, R.V., Gruener, J.E., Amils, R., and Knoll, A.H. (2005) The Río
777 Tinto Basin, Spain: Mineralogy, sedimentary geobiology, and implications for interpretation
778 of outcrop rocks at Meridiani Planum, Mars. Earth and Planetary Science Letters, 240(1),
779 149-167.

780 Fernández-Remolar, D.C., Preston, L.J., Sánchez-Román, M., Izawa, M.R.M., Huang, L., Southam,
781 G., Banerjee, N.R., Osinski, G.R., Flemming, R., Gómez-Ortíz, D., Prieto-Ballesteros, O.,
782 Rodríguez, N., Amils, R., and Dyar, M.D. (2012) Carbonate precipitation under bulk acidic
783 conditions as a potential biosignature for searching life on Mars. Earth and Planetary Science
784 Letters, 351, 13-26.

785 Fernández-Remolar, D.C., Prieto-Ballesteros, O., Gómez-Ortíz, D., Fernández-Sampedro, M.,
786 Sarrazin, P., Gailhanou, M., and Amils, R. (2011) Río Tinto sedimentary mineral
787 assemblages: A terrestrial perspective that suggests some formation pathways of
788 phyllosilicates on Mars. Icarus, 211(1), 114-138.

789 Fernández-Remolar, D.C., Prieto-Ballesteros, O., Rodríguez, N., Gómez, F., Amils, R., Gómez-
790 Elvira, J., and Stoker, C.R. (2008) Underground Habitats in the Río Tinto Basin: A Model for
791 Subsurface Life Habitats on Mars. Astrobiology, 8(5), 1023-1047.

792 Fernández-Remolar, D., Rodríguez, N., Gómez, F., and Amils, R. (2003) The geological record of an
793 acidic environment driven by iron hydrochemistry: The Tinto River system. Journal of
794 Geophysical Research, 108(E7), 10.1029/2002JE001918.

795 García-Moyano, A., González-Toril, E., Aguilera, Á., and Amils, R. (2012) Comparative microbial
796 ecology study of the sediments and the water column of the Río Tinto, an extreme acidic
797 environment. FEMS Microbiology Ecology, 81(2), 303-314.

798 Goldstein, J., Newbury, D.E., Joy, D.C., Lyman, C.E., Echlin, P., Lifshin, E., Sawyer, L., and
799 Michael, J.R. (2003) Scanning Electron Microscopy and X-ray Microanalysis. Springer
800 Science and Business Media, New York.

801 Gómez-Ortiz, D., Fernández-Remolar, D.C., Granda, Á., Quesada, C., Granda, T., Prieto-Ballesteros,
802 O., Molina, A., and Amils, R. (2014) Identification of the subsurface sulfide bodies
803 responsible for acidity in Río Tinto source water, Spain. Earth and Planetary Science Letters,
804 391, 36-41.

805 González-Toril, E.F., Llobet-Brossa, E., Casamayor, E.O., Amann, R., and Amils, R. (2003)
806 Microbial ecology of an extreme acidic environment, the Tinto River. Applied and
807 Environmental Microbiology, 69(8), 4853-4865.

808 Grotzinger, J.P., and Milliken, R.E. (2012) The Sedimentary Rock Record of Mars. Sedimentary
809 Geology of Mars, 102, p. 1-48. SEPM Society for Sedimentary Geology.

Herschy, B., Whicher, A., Camprubi, E., Watson, C., Dartnell, L., Ward, J., Evans, J.R.G., and Lane, N. (2014) An Origin-of-Life Reactor to Simulate Alkaline Hydrothermal Vents. Journal of Molecular Evolution, 79(5), 213-227.

Edwards, K.J., Goebel, B.M., Rodgers, T.M., Schrenk, M.O., Gihring, T.M., Cardona, M.M., Mcguire, M.M., Hamers, R.J., Pace, N.R., and Bandfield, J.F. (1999) Geomicrobiology of Pyrite (FeS_2) Dissolution: Case Study at Iron Mountain, California. Geomicrobiology Journal, 16(2), 155-179.

King, P.L., and McLennan, S.M. (2010) Sulfur on Mars. Elements, 6(2), 107.

Knoll, A.H., Canfield, D.E., and Konhauser, K.O. (2012) Fundamentals of geobiology. Blackwell Publishing Ltd, Oxford, UK.

Lane, N., and Martin, W.F. (2012) The origin of membrane bioenergetics. Cell, 151, 1406-1416.

Leistel, J.M., Marcoux, E., Thiéblemont, D., Quesada, C., Sánchez, A., Almodóvar, G.R., Pascual, E., and Sáez, R. (1998) The volcanic-hosted massive sulphide deposits of the Iberian Pyrite Belt. Mineralium Deposita, 33(2), 2-30.

Leybourne, M.I., Hamilton, S.M., Mwenifumbo, C.J., Goodfellow, W.D., and Boyle, D.R. (2009) Hydrogeochemical and geophysical evidence for borehole oxidation of massive sulphides below the water table and generation of self-potential anomalies. Geochemistry: Exploration, Environment, Analysis, 9, 39-50.

Malki, M., de Lacey, A.L., Rodríguez, N., Amils, R., and Fernandez, V.M. (2008) Preferential Use of an Anode as an Electron Acceptor by an Acidophilic Bacterium in the Presence of Oxygen. Applied and Environmental Microbiology, 74(14), 4472-4476.

Malki, M., González-Toril, E., Sanz, J.L., Gómez, F., Rodríguez, N., and Amils, R. (2006) Importance of the iron cycle in biohydrometallurgy. Hydrometallurgy, 83(1–4), 223-228.

McCubbin, F.M., Tosca, N.J., Smirnov, A., Nekvasil, H., Steele, A., Fries, M., and Lindsley, D.H. (2009) Hydrothermal jarosite and hematite in a pyroxene-hosted melt inclusion in martian meteorite Miller Range (MIL) 03346: Implications for magmatic-hydrothermal fluids on Mars. Geochimica et Cosmochimica Acta, 73(16), 4907-4917.

Michalski, J.R., Cuadros, J., Niles, P.B., Parnell, J., Deanne Rogers, A., and Wright, S.P. (2013) Groundwater activity on Mars and implications for a deep biosphere. Nature Geosci, 6(2), 133-138.

Michalski, J.R., Dobrea, E.Z.N., Niles, P.B., and Cuadros, J. (2017) Ancient hydrothermal seafloor deposits in Eridania basin on Mars. Nature Communications, 8, 15978.

Molina, A., López, I., Prieto-Ballesteros, O., Fernández-Remolar, D., de Pablo, M.Á., and Gómez, F. (2017) Coogoon Valles, western Arabia Terra: Hydrological evolution of a complex Martian channel system. Icarus, 293(Supplement C), 27-44.

Nachon, M., Clegg, S.M., Mangold, N., Schröder, S., Kah, L.C., Dromart, G., Ollila, A., Johnson, J.R., Oehler, D.Z., Bridges, J.C., Le Mouélic, S., Forni, O., Wiens, R.C., Anderson, R.B., Blaney, D.L., Bell, J.F., Clark, B., Cousin, A., Dyar, M.D., Ehlmann, B., Fabre, C., Gasnault, O., Grotzinger, J., Lasue, J., Lewin, E., Léveillé, R., McLennan, S., Maurice, S., Meslin, P.Y., Rapin, W., Rice, M., Squyres, S.W., Stack, K., Sumner, D.Y., Vaniman, D., and Wellington, D. (2014) Calcium sulfate veins characterized by ChemCam/Curiosity at Gale crater, Mars. Journal of Geophysical Research: Planets, 119(9), 1991-2016.

Nordstrom, D.K., Alpers, C.N., Ptacek, C.J., and Blowes, D.W. (2000) Negative pH and extremely acidic mine waters from Iron Mountain, California. Environmental Science & Technology, 34, 254-258.

Oggerin, M., Tornos, F., Rodríguez, N., De Moral, C., and Sánchez-Román, M. (2013) Specific jarosite biomineralization by Purpureocillium lilacinum, an acidophilic fungi isolated from Río Tinto. Environmental Microbiology, 15, 2228-2237.

Ohmura, N., Sasaki, K., Matsumoto, N., and Saiki, H. (2002) Anaerobic respiration using Fe^{3+}, S^0 and H_2 in the chemolithoautotrophic bacterium. Journal of Bacteriology, 18, 2081–2087.

Oliveira, J.T. (1990) Stratigraphy and syn-sedimentary tectonism in the South Portuguese Zone. In R.D. Dallmeyer, and E. Martínez García, Eds. Pre-Mesozoic Geology of Iberia, p. 334-347. Springer Verlang, Berlin.

Peretyazhko, T., Zachara, J.M., Boily, J.F., Xia, Y., Gassman, P.L., Arey, B.W., and Burgos, W.D. (2009) Mineralogical transformations controlling acid mine drainage chemistry. Chemical Geology, 262(3), 169-178.

Puente-Sánchez, F., Moreno-Paz, M., Rivas, L.A., Cruz-Gil, P., García-Villadangos, M., Gómez, M.J., Postigo, M., Garrido, P., González-Toril, E., Briones, C., Fernández-Remolar, D., Stoker, C., Amils, R., and Parro, V. (2014) Deep subsurface sulfate reduction and methanogenesis in the Iberian Pyrite Belt revealed through geochemistry and molecular biomarkers. Geobiology, 12(1), 34-47.

Quesada, C. (1991) Geological constraints on the Paleozoic tectonic evolution of tectonostratigraphic terranes in the Iberian Massif. Tectonophysics, 185, 225-245.

Quesada, C. (1998) A reappraisal of the structure of the Spanish segment of the Iberian Pyrite Belt. Mineralium Deposita, 33, 31-44.

Rodriguez-Navarro, C., Jroundi, F., Schiro, M., Ruiz-Agudo, E. and González-Muñoz, M.T. (2012) Influence of Substrate Mineralogy on Bacterial Mineralization of Calcium Carbonate: Implications for Stone Conservation. Applied and Environmental Microbiology, 78, 4017-4029.

Sánchez-Andrea, I., Rodríguez, N., Amils, R., and Sanz, J.L. (2011) Microbial Diversity in Anaerobic Sediments at Río Tinto, a Naturally Acidic Environment with a High Heavy Metal Content. Applied and Environmental Microbiology, 77(17), 6085-6093.

Sánchez-Román, M., Puente-Sánchez, F., Parro, V., and amils, R. (2015) Nucleation of Fe-rich phosphates and carbonates on microbial cells and exopolymeric substances. Frontiers in Microbiology, 6, 1024.

Sand, W., Gehrke, T., Jozsa, P.-G., and Schippers, A. (2001) (Bio)chemistry of bacterial leaching--direct vs. indirect bioleaching. Hydrometallurgy, 59(2-3), 159-175.

Sholes, S.F., Smith, M.L., Claire, M.W., Zahnle, K.J., and Catling, D.C. (2017) Anoxic atmospheres on Mars driven by volcanism: Implications for past environments and life. Icarus, 290, 46-62.

Stoker, C.R., Cannon, H.N., Dunagan, S.E., Lemke, L.G., Glass, B.J., Miller, D., Gomez-Elvira, J., Davis, K., Zavaleta, J., Winterholler, A., Roman, M., Rodriguez-Manfredi, J.A., Bonaccorsi, R., Bell, M.S., Brown, A., Battler, M., Chen, B., Cooper, G., Davidson, M., Fernández-Remolar, D., Gonzales-Pastor, E., Heldmann, J.L., Martínez-Frías, J., Parro, V., Prieto-Ballesteros, O., Sutter, B., Schuerger, A.C., Schutt, J., and Rull, F. (2008) The 2005 MARTE Robotic Drilling Experiment in Río Tinto, Spain: Objectives, Approach, and Results of a Simulated Mission to Search for Life in the Martian Subsurface. Astrobiology, 8(5), 921-945.

Simoneit, B.R.T. (2004) Prebiotic organic synthesis under hydrothermal conditions: an overview. Advances in Space Research, 33(1), 88-94.

Vaniman, D.T., Bish, D.L., Ming, D.W., Bristow, T.F., Morris, R.V., Blake, D.F., Chipera, S.J., Morrison, S.M., Treiman, A.H., Rampe, E.B., Rice, M., Achilles, C.N., Grotzinger, J.P., McLennan, S.M., Williams, J., Bell, J.F., Newsom, H.E., Downs, R.T., Maurice, S., Sarrazin, P., Yen, A.S., Morookian, J.M., Farmer, J.D., Stack, K., Milliken, R.E., Ehlmann, B.L., Sumner, D.Y., Berger, G., Crisp, J.A., Hurowitz, J.A., Anderson, R., Des Marais, D.J., Stolper, E.M., Edgett, K.S., Gupta, S., and Spanovich, N. (2014) Mineralogy of a Mudstone at Yellowknife Bay, Gale Crater, Mars. Science, 343(6169).

Wadhwa, M. (2008) Redox conditions on small bodies, the Moon and Mars. Reviews in Mineralogy & Geochemistry, 68, 493-510.

907 Wang, X., Ouyang, Z., Zhuo, S., Zhang, M., Zheng, G., and Wang, Y. (2014) Serpentinization,
908 abiogenic organic compounds, and deep life. Science China Earth Sciences, 57(5), 878-887.

909 Wächtershäuser, G. (1992) Groundworks for an evolutionary biochemistry: The iron-sulphur world.
910 Progress in Biophysics and Molecular Biology, 58(2), 85-201.

911 Welch, S.A., and Vandevivere, P. (1994) Effect of microbial and other naturally occurring polymers
912 on mineral dissolution. Geomicrobiology Journal, 12(4), 227-238.

913 Zhou, Y., Wang, R., and Lu, X. (2011) Anorthite dissolution promoted by bacterial adhesion: Direct
914 evidence from dialytic experiment. Science China Earth Sciences, 54(2), 204-211.

915 Zhu, T., and Dittrich, M. (2016) Carbonate Precipitation through Microbial Activities in Natural
916 Environment, and Their Potential in Biotechnology: A Review. Frontiers in Bioengineering
917 and Biotechnology, 4, 4.

918

919

920 **FIGURE CAPTIONS**

921

922 **FIGURE 1.** Composite image showing the distribution of boreholes 4, 8, 10 and 11 (BH4, BH8, BH10
923 and BH11) that drilled to sample the basement of the terrestrial Mars analog of the Río Tinto. The
924 lithology, faults, key minerals, sulfate content in the rock and the main types of microbial structures
925 are indicated.

926

927 **FIGURE 2.** Diverse mineralized microstructures found on the surfaces of quartz and pyrite that show
928 evidence of active mineral attack. (**a**) Discoidal to vermicular carbon-rich structures covering a quartz
929 surface that are associated with Fe sulfates (FeS) in sample 4-19a, found at a depth of 41 meters (see
930 main EDAX peaks for S, O, Fe, Si and C shown in **a1**). (**b**) Oval-like C-bearing bodies spread over a
931 quartz surface in sample 4-18a (37.4 m). (**c**) Carbon-rich microstructures found in sample 4-54b
932 (depth of 134.5 m) associated with nanoscale pits (white arrows), suggesting biomineralized
933 nanobacteria and pits that could be the result of microbial attack. (**d** and **e**) Very dense network of C-
934 bearing sinuous threads resembling exopolymers found on the interior and surface of pyrite (unique
935 peaks of S and Fe in **d1**) in samples 4-46b and 4-59b, at depths of 115.45 and 150 meters,
936 respectively. The peak at 2.2 keV corresponds to Au coating for sample preparation.

937

938 **FIGURE 3.** Very distinctive mineralized structures (157.5 m) recovered from BH4, which are
939 associated with barite and pyrite surfaces and where filaments (f) and dark dots (dd) are observed. (**a**)
940 Tightly packed covering of oval-like, C-bearing structures on a pyrite surface found in sample 4-67a
941 that occasionally are arranged forming linear clusters (lc). (**b**) Remnants of carbonaceous straight
942 filamentous microstructures occurring as ovoides to elongated structures (f) on a barite crystal surface
943 in sample 4-67a after being exposed to the SEM electron beam, which suggests the occurrence of
944 organic carbon. (**c**) Same as in (**b**), showing the remnants of totally obliterated filaments occurring as
945 dark dots (dd) covering the barite surface (**c1**). (**c1**) EDAX spectrum that suggests the occurrence of
946 filaments mineralized (fm) to Fe-carbonate (EDAX peaks of C, O and Fe) infilling a micron-sized
947 cavity in the barite surface (EDAX peaks of S, O and Ba). (**d**) SEM image showing th occurrence of
948 similar filaments that have been mineralized (fm) to Fe-carbonates and some carbonaceous remnants
949 (f) of partially obliterated filaments. (**e**) Intact upright filaments (f) covering the barite surface at 157.5
950 m. These filaments that have been most frequently obliterated to form tiny carbon-rich bodies after
951 being exposed to the SEM beam.

952

953 **Figure 4.** Linear clusters mineralized by Fe-carbonate (siderite) in sample 4-67a (157.5 m).
954 Spectrum **a** shows an elemental composition of the mineralized clusters consistent with a siderite
955 (major X-ray peaks for C, Fe, O, and S) intermixed with small amounts of S-bearing compounds like
956 elemental sulfur or pyrite. Spectrum **b** shows an elemental composition consistent with barite (major
957 X-ray peaks for S, O and Ba) that is covered by carbonaceous remnants. This is supported by a high
958 concentration of carbon (semi-quantitatively estimated at ~42 atomic percent, but with significant
959 uncertainty). The presence of a coating of carbon-rich organic matter attenuates the fluorescent X-
960 rays, with a greater attenuation for the lower-energy O and S X-rays than for Ba, which increases the
961 uncertainty in the (semi)quantification by the EDAX software. However, the qualitative interpretation

of the X-ray spectra strongly supports the identification of barite with a coating of organic materials. High peak at 2.2 keV placed at the left of S correspond to Au peak coming from the conductive coating. Peaks at 1.7 and 2.7 keV are also from the coating conductive material and correspond to Au and Pd respectively.

FIGURE 5. Occurrence of ferric oxides detected by EDAX (**a1** and **b1**) in the upper part of borehole BH4, suggesting aerobic conditions for the uppermost region of the Río Tinto basement. (**a**) Sample 4-9a collected at a depth of 19 m, showing colomorphic mineral structures (**a1**) of iron oxides. (**b**) Sample 4-16a recovered at 32 meters from BH4 that has a framework of crosscutting veins, in which interspaces are filled with colomorphic iron oxides (**b1**). Spectra a1 and b1 were collected from the total area scanned by SEM. The high peak at 2.2 keV placed at the left of S correspond to Au from the conductive coating which label has been removed. Peaks at 1.7 and 2.7 keV come from the coating conductive material and correspond to Au and Pd respectively.

FIGURE 6. Pyrite crystals with clear traces of microbial oxidation and precipitation by-products as oxidized phases (FeS) that could correspond to ferric sulfates. (**a**, and **b**) Samples BH11_36.11 and BH10_125.75 collected in BH11 and BH10 at 36.11 and 125.75-meter depths, respectively, showing evidence of advanced and incipient corrosion on the pyrite surfaces by oxidation of sulfur and iron to form rosettes (FeS) and amorphous patches. Squares mark the incipient corrosion (**b**) in pyrites found in sample BH10_125.75. (**c**) EDAX analysis of a full SEM image (**c1**) of a degraded pyrite found in sample BH10_125.75 and completely coated by a ferric sulfate. (**d**) Occurrence of ferric sulfate crystals confirmed by EDAX (**d1**) in sample 4-18a that was collected at a depth of 37.5 m. Peaks at 0.7 and 2.2 keV come from the coating conductive material and correspond to Co and Au respectively.

FIGURE 7. Barite crystals of hydrothermal origin (~ 345 Ma) found in different areas of the Río Tinto basement that show evident signs of corrosion and precipitation of secondary minerals. (**a**) Association of a corroded crystal of barite (ba) with iron oxides (io), quartz (qz) and Fe-carbonate (see C peak in **a1**), found in sample 4-32a at a depth of 77 m; dashed lines trace the boundary between iron oxides (io) and quartz (qz). (**b**) SEM image of a prismatic barite crystal (**b1**) in sample 4-50b (126 m deep) that has been exposed to local attack at several microsites (some examples of dissolution fronts are traced by dashed lines) followed by the precipitation of complex Fe-carbonate spheroids (**b2**). Unlabelled peak at 2.2 keV placed at the lef of S peak is from the coating conductive material and correspond to Au. Smaller unlabelled peaks starting at 2.9 keV correspond to Pd is from the coating material as well.

FIGURE 8. Identification of barite crystals in BH4 and BH8 with signs of advanced corrosion. (**a**) Detail of contact between a corroded barite surface (Ba) and an Fe-carbonate (FeCO3) complex labelled as FeC with a filamentous microstructure that are separated by an interspace (is) (sample 4-67a collected at 157.5 m); the barite surface shows a characteristic dotted pattern. (**a1**) EDAX spectrum obtained from the area in (**a)** showing C, O, Fe and Ba peaks that are consistent with the occurrence of barite, Fe-carbonate and traces of organic compounds. (**b**) Sample 8-68c collected at a

depth of 163 m showing a quartz void (qz) that is filled with remnants of barite crystals (ba) embedded in a matrix of spheroid intergrowths of Fe-carbonates (FeC) with filamentous microfabric. (**b1**) EDAX spectrum of the full image showing C, O, Fe, and Ba peaks consistent with the co-occurrence of barite and Fe-carbonate. Unlabelled peak at 2.2 ans 2.9 keV placed at the right of Si peak come from the coating conductive material and correspond to Au and Pd, respectively.

FIGURE 9. Association of Fe-carbonate with pyrite and quartz in deeper regions of the Río Tinto basement in boreholes BH4 and BH8. (**a**) Sample 4-55c collected at 139 m that shows a pyrite crystal embedded in a mass of complex Fe-carbonate spheroids (**a1**); while the pyrite rhombohedrum has an irregular surface, the Fe-carbonate spheroids do not intrude into the sulfide crystal. (**b**) Fe-carbonate spheroids and disc-shaped laminar Fe-carbonate growing on a pyrite crystal, observed in sample 8-66a at 155 m. (**c**) Sample 4-52fg collected at a depth of 131.5 m displaying spheroidal Fe-carbonate (FeC) that grows on a pyrite surface (py) with no evidence of attack and intrusion by the carbonate. (**c1**) EDAX spectrum of an Fe-carbonate spheroid that is shaped by a faceted void of the pyrite surface. (**d**) Sample 4-60a (152 m depth) showing an amalgamation of disc-shaped laminas of Fe-carbonate (**d1**) covering a chlorite rich matrix (**d2**).

FIGURE 10. Drawing outlining the microbial attack on a sulfate surface through the mobilization of sulfate anion to sulfide by SRB from the barite surface that results in the formation of Fe-carbonate. The sulfate would mobilize entry into the metabolic machinery by acidic leaching of organic acids released by microbes (e.g., HCOOH). The process could likely be favored by the emergence of a pH gradient that would concentrate the bicarbonate in the outermost area of the biofilm. Such configuration would promote the precipitation and thickening of carbonates once the microbial attack is progressing.

This is a preprint, the final version is subject to change, of the American Mineralogist (MSA)
Cite as Authors (Year) Title. American Mineralogist, in press.
DOI: http://dx.doi.org/10.2138/am-2018-6288

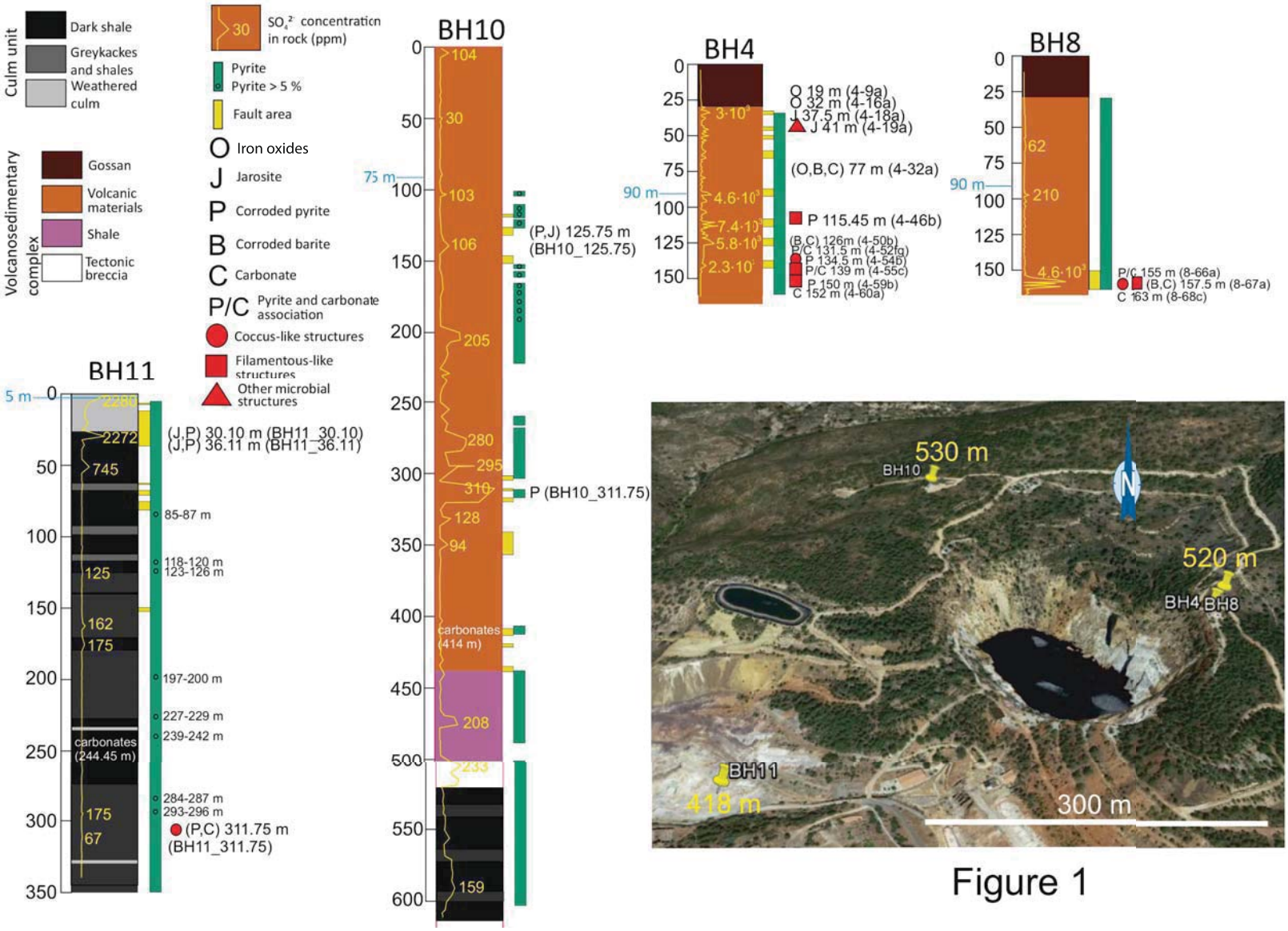

Figure 1

This is a preprint, the final version is subject to change, of the American Mineralogist (MSA)
Cite as Authors (Year) Title. American Mineralogist, in press.
DOI: http://dx.doi.org/10.2138/am-2018-6288

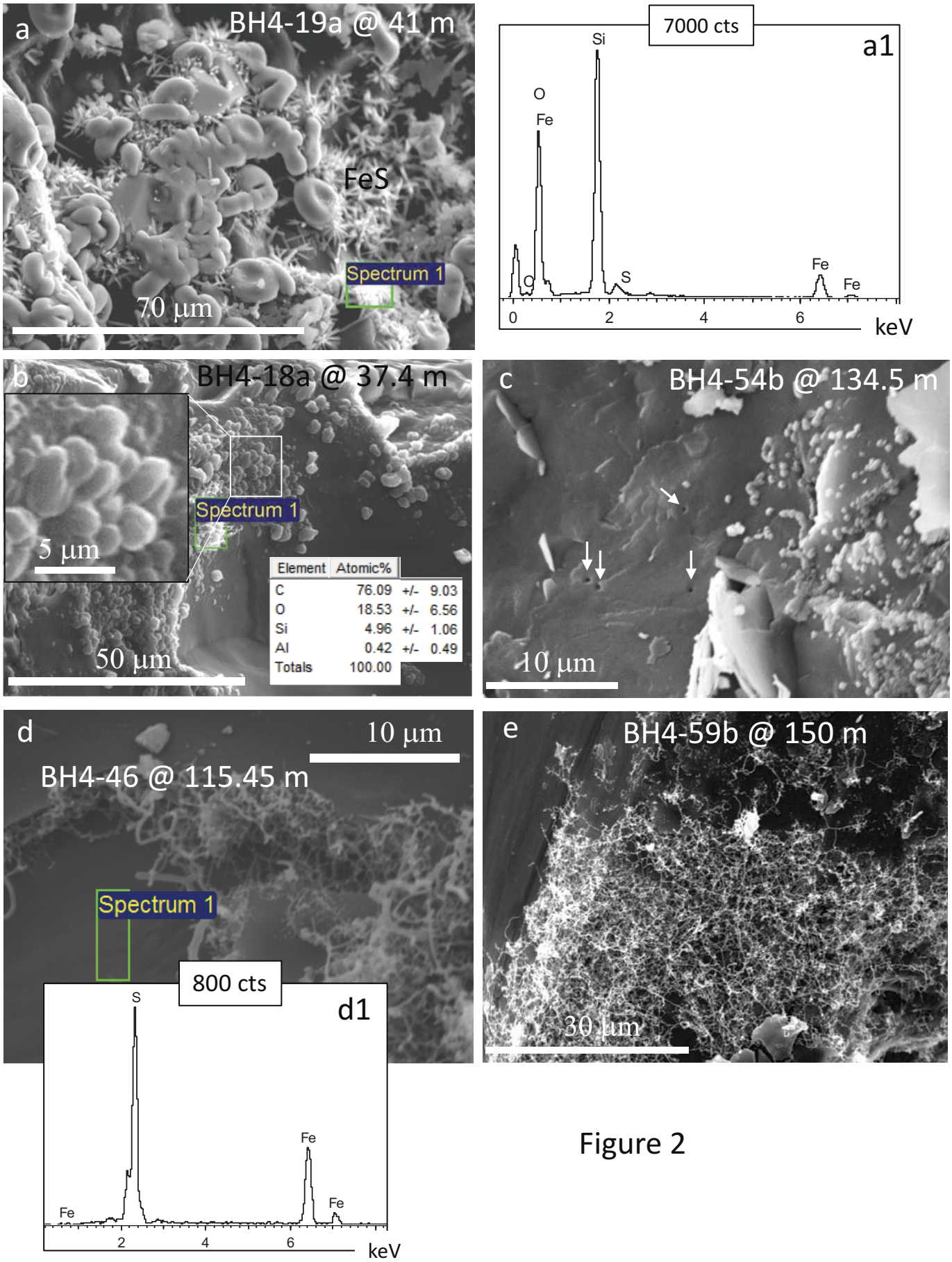

Figure 2

This is a preprint, the final version is subject to change, of the American Mineralogist (MSA)
Cite as Authors (Year) Title. American Mineralogist, in press.
DOI: http://dx.doi.org/10.2138/am-2018-6288

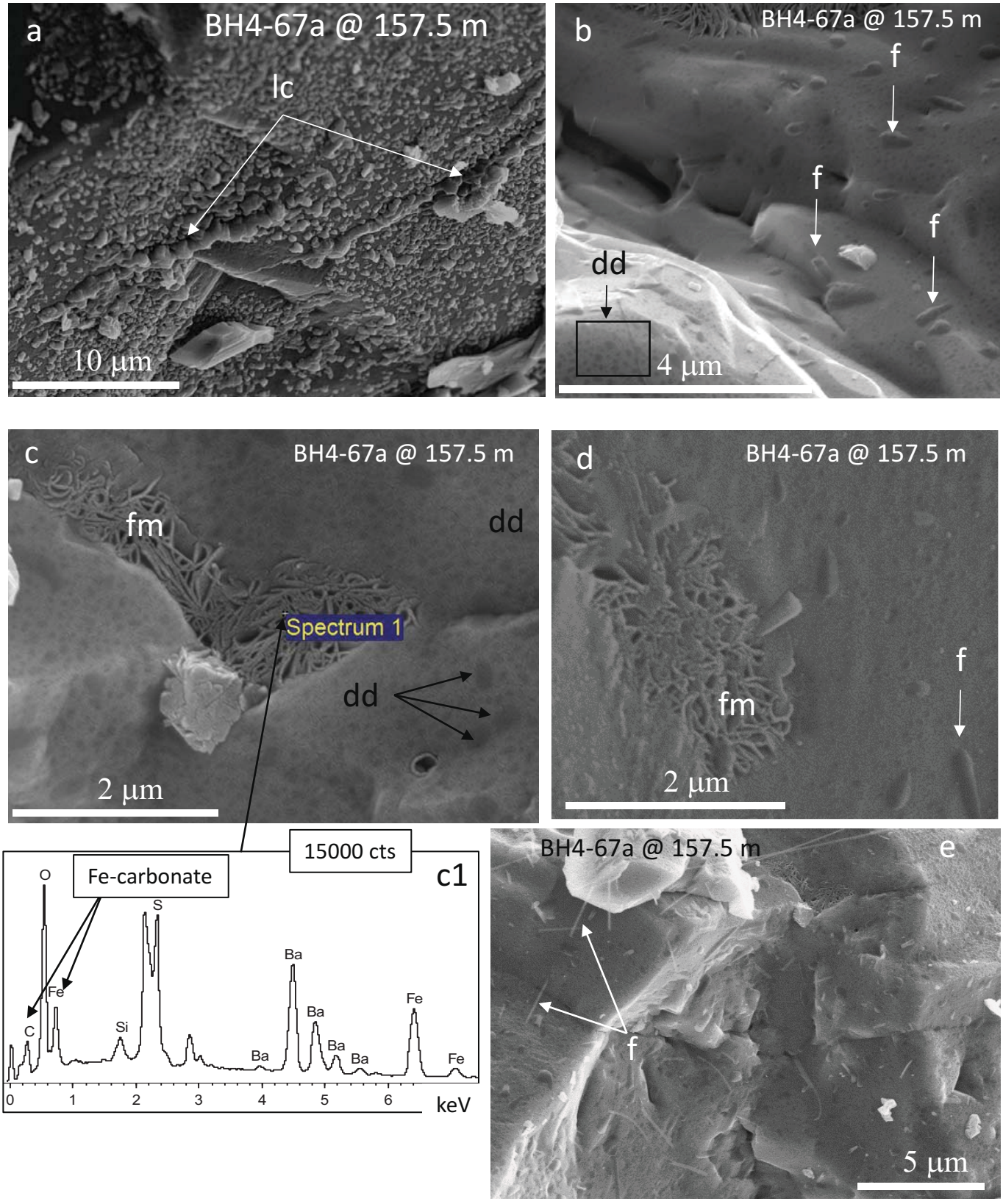

Figure 3

This is a preprint, the final version is subject to change, of the American Mineralogist (MSA)
Cite as Authors (Year) Title. American Mineralogist, in press.
DOI: http://dx.doi.org/10.2138/am-2018-6288

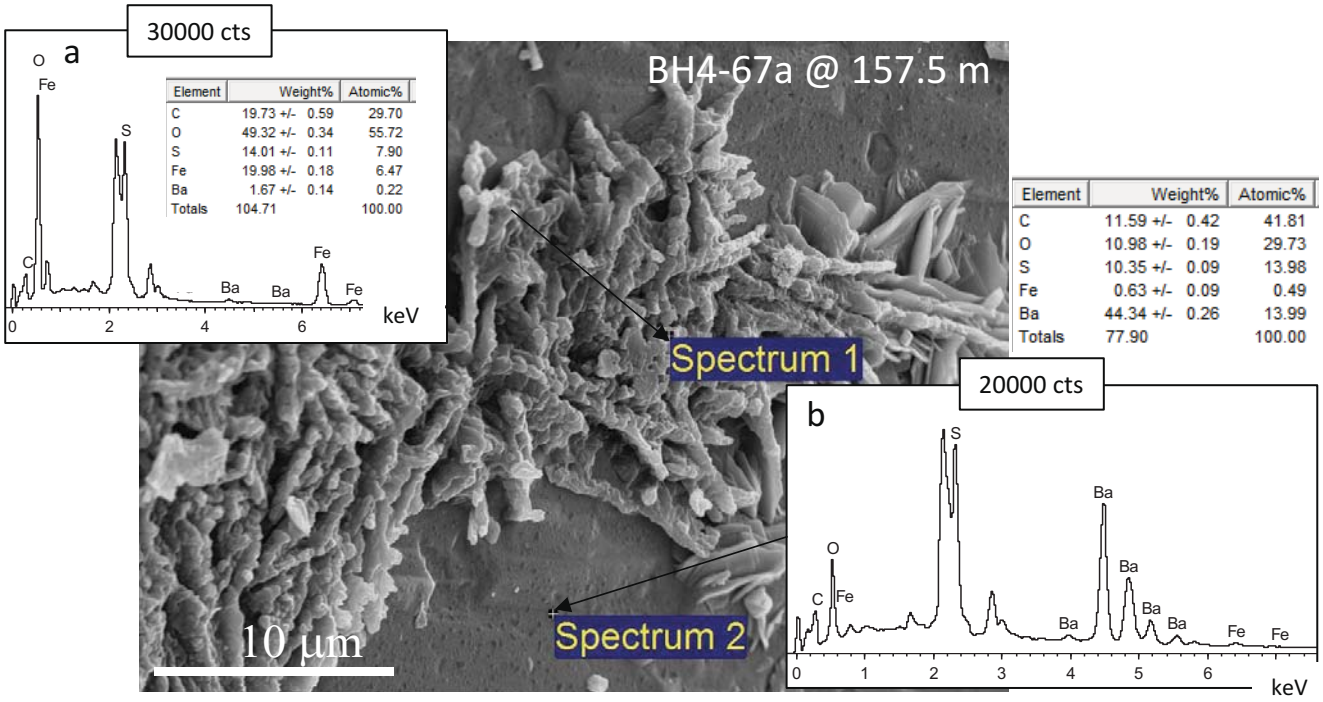

Figure 4

This is a preprint, the final version is subject to change, of the American Mineralogist (MSA)
Cite as Authors (Year) Title. American Mineralogist, in press.
DOI: http://dx.doi.org/10.2138/am-2018-6288

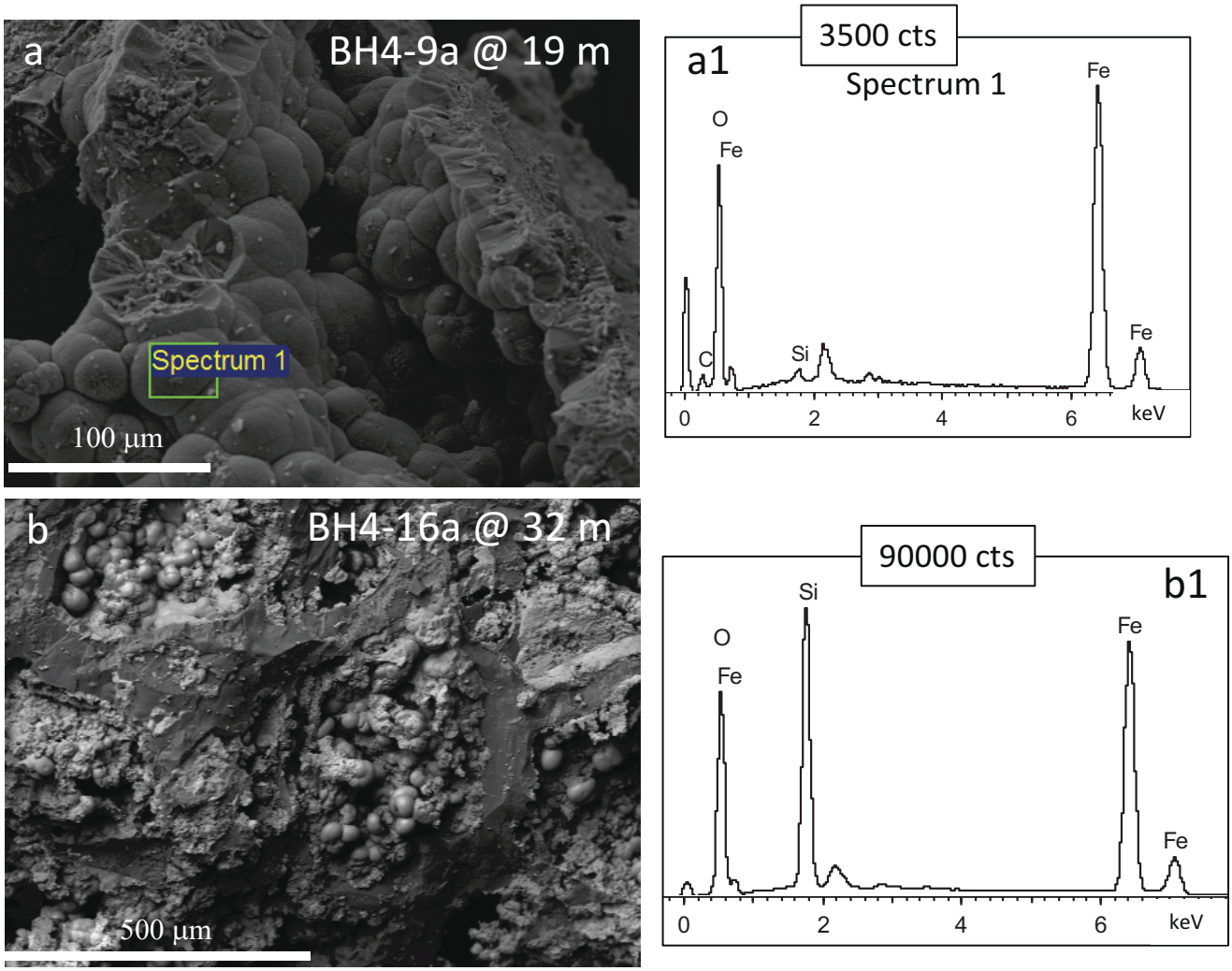

Figure 5

This is a preprint, the final version is subject to change, of the American Mineralogist (MSA)
Cite as Authors (Year) Title. American Mineralogist, in press.
DOI: http://dx.doi.org/10.2138/am-2018-6288

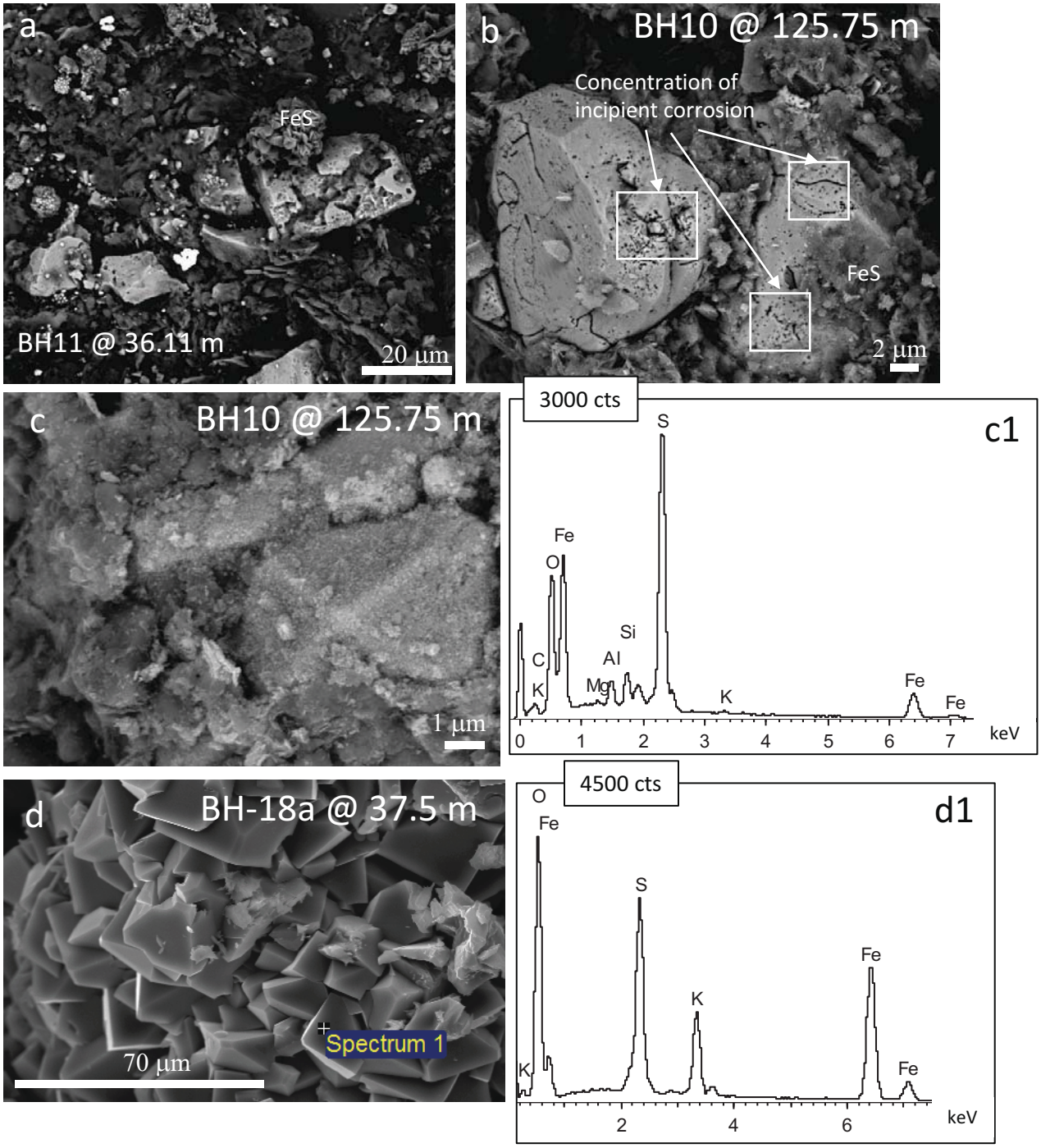

Figure 6

This is a preprint, the final version is subject to change, of the American Mineralogist (MSA)
Cite as Authors (Year) Title. American Mineralogist, in press.
DOI: http://dx.doi.org/10.2138/am-2018-6288

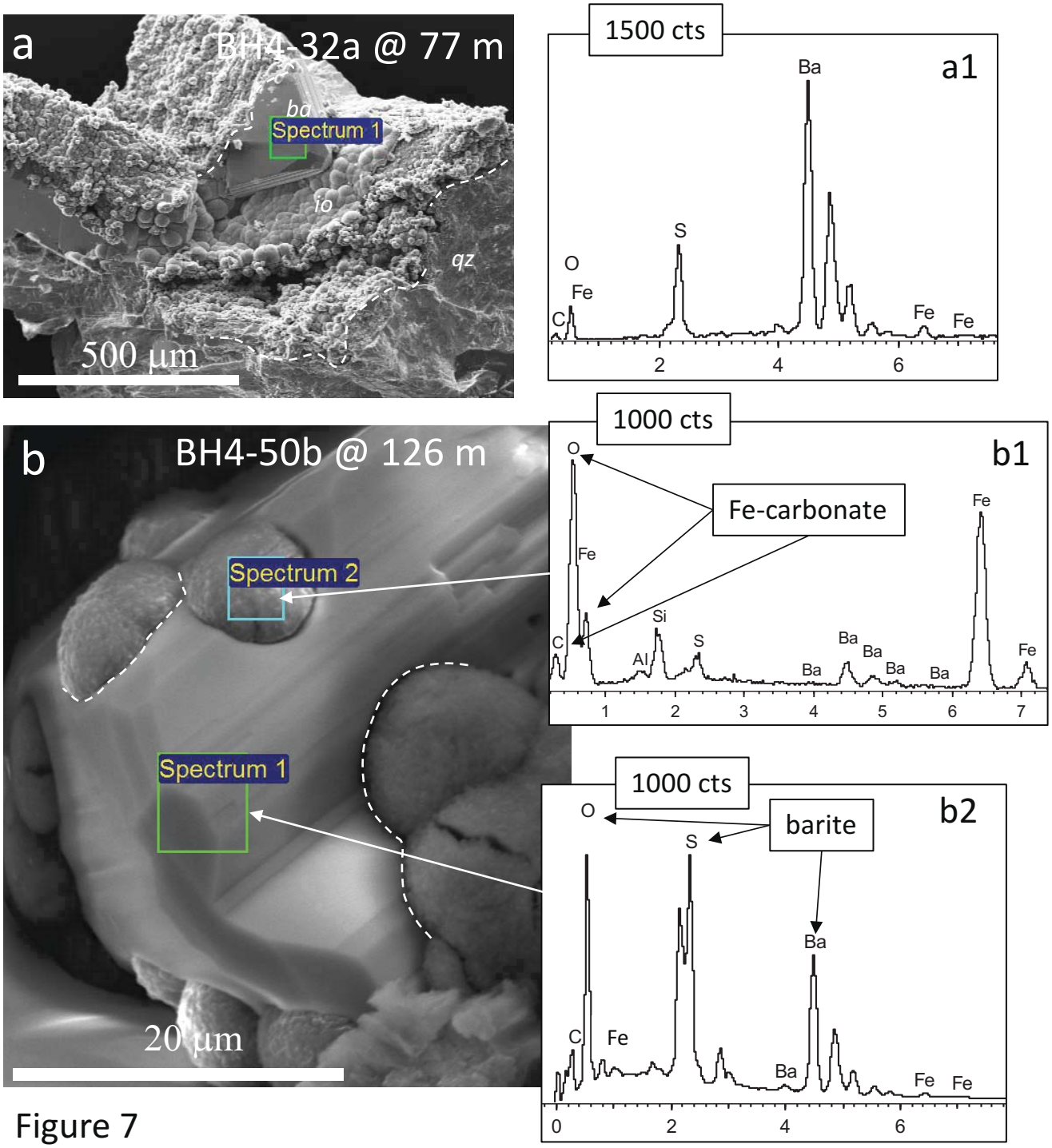

Figure 7

This is a preprint, the final version is subject to change, of the American Mineralogist (MSA)
Cite as Authors (Year) Title. American Mineralogist, in press.
DOI: http://dx.doi.org/10.2138/am-2018-6288

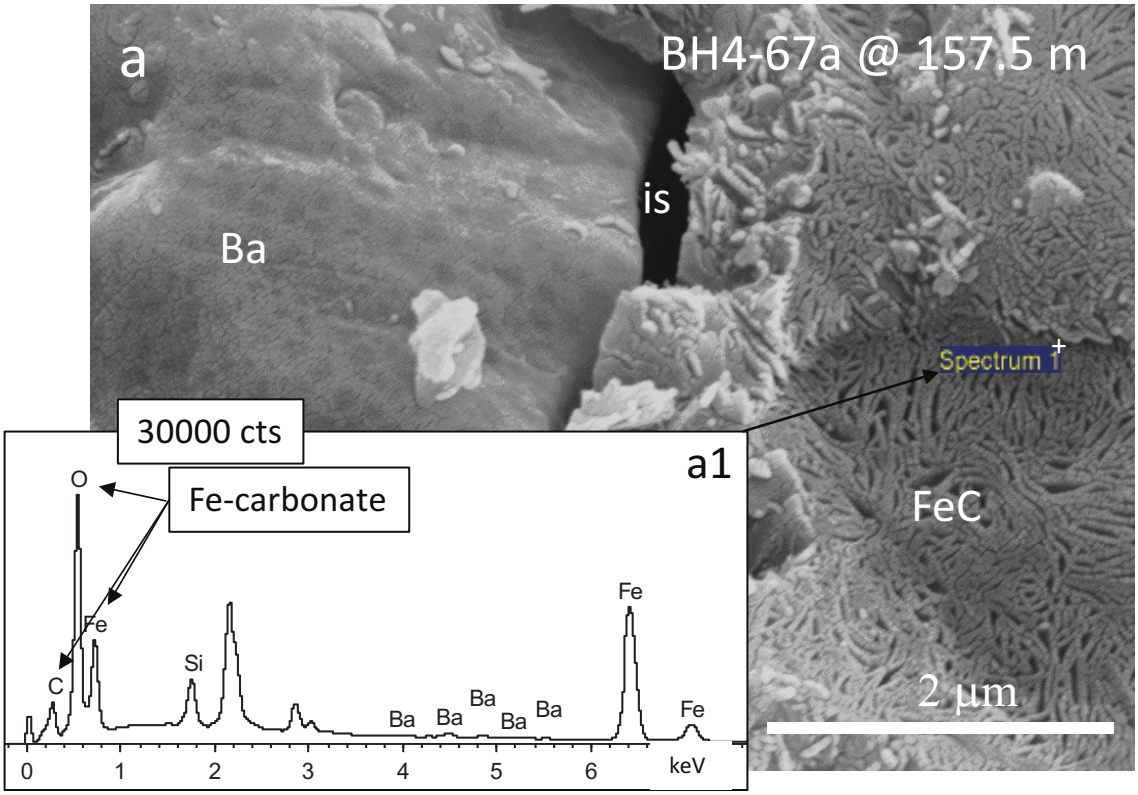

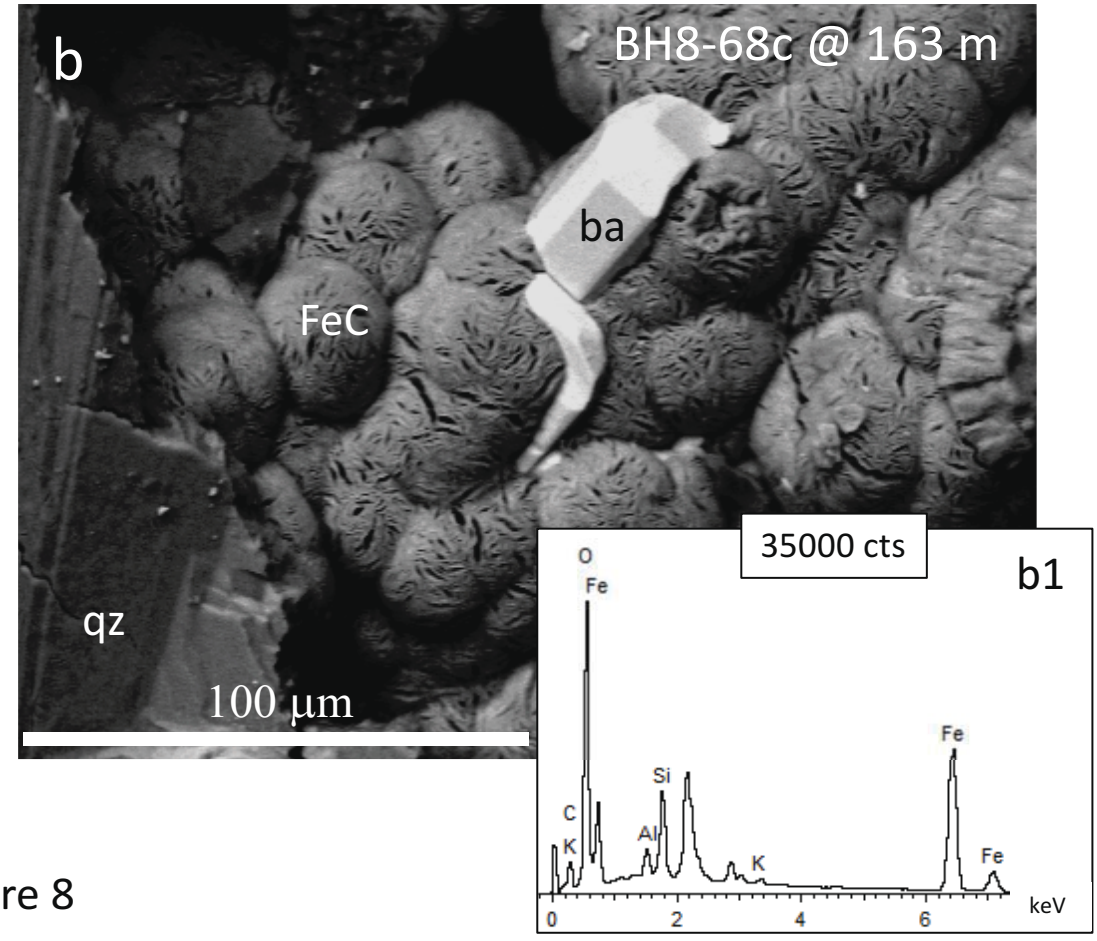

Figure 8

This is a preprint, the final version is subject to change, of the American Mineralogist (MSA)
Cite as Authors (Year) Title. American Mineralogist, in press.
DOI: http://dx.doi.org/10.2138/am-2018-6288

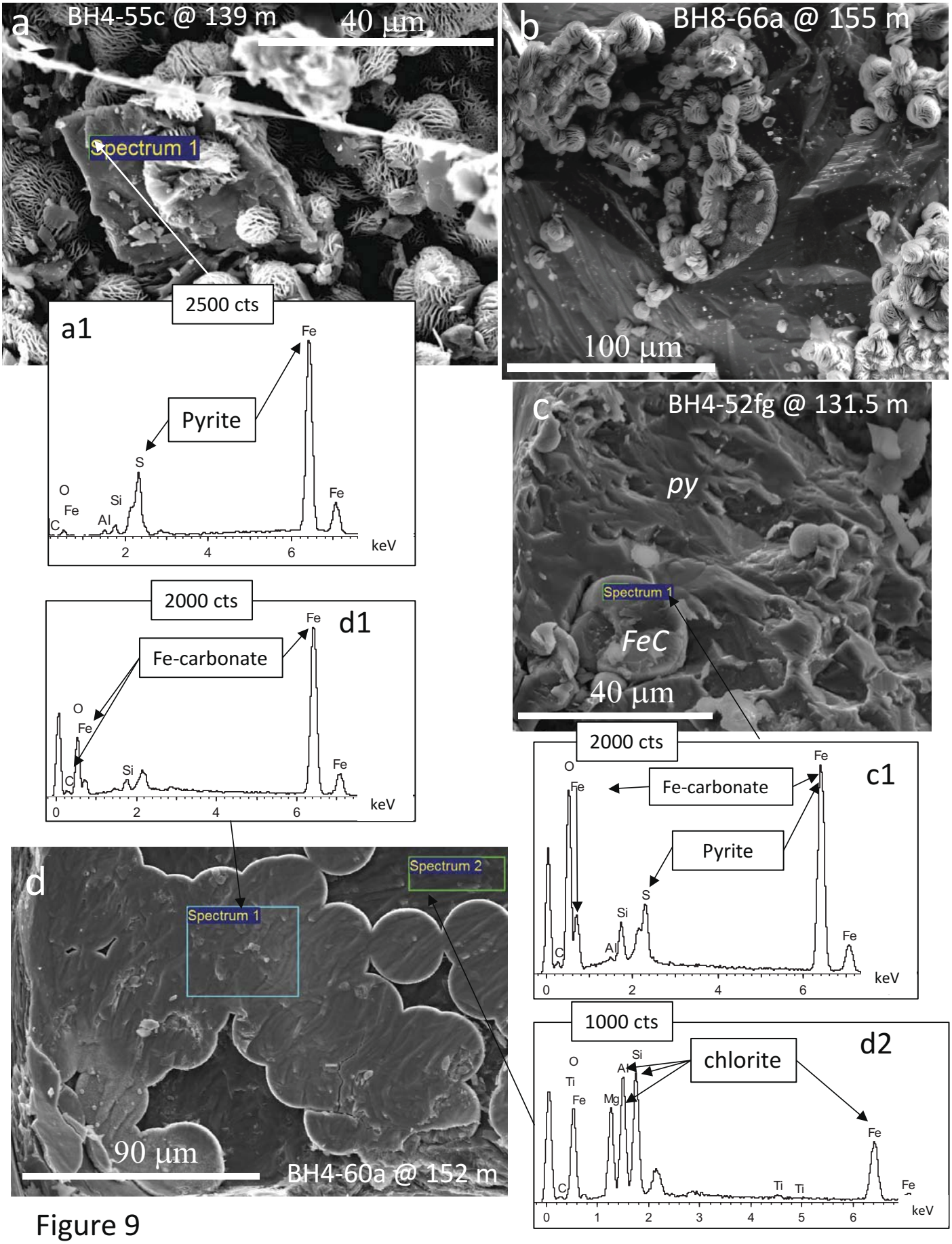

Figure 9

This is a preprint, the final version is subject to change, of the American Mineralogist (MSA)
Cite as Authors (Year) Title. American Mineralogist, in press.
DOI: http://dx.doi.org/10.2138/am-2018-6288

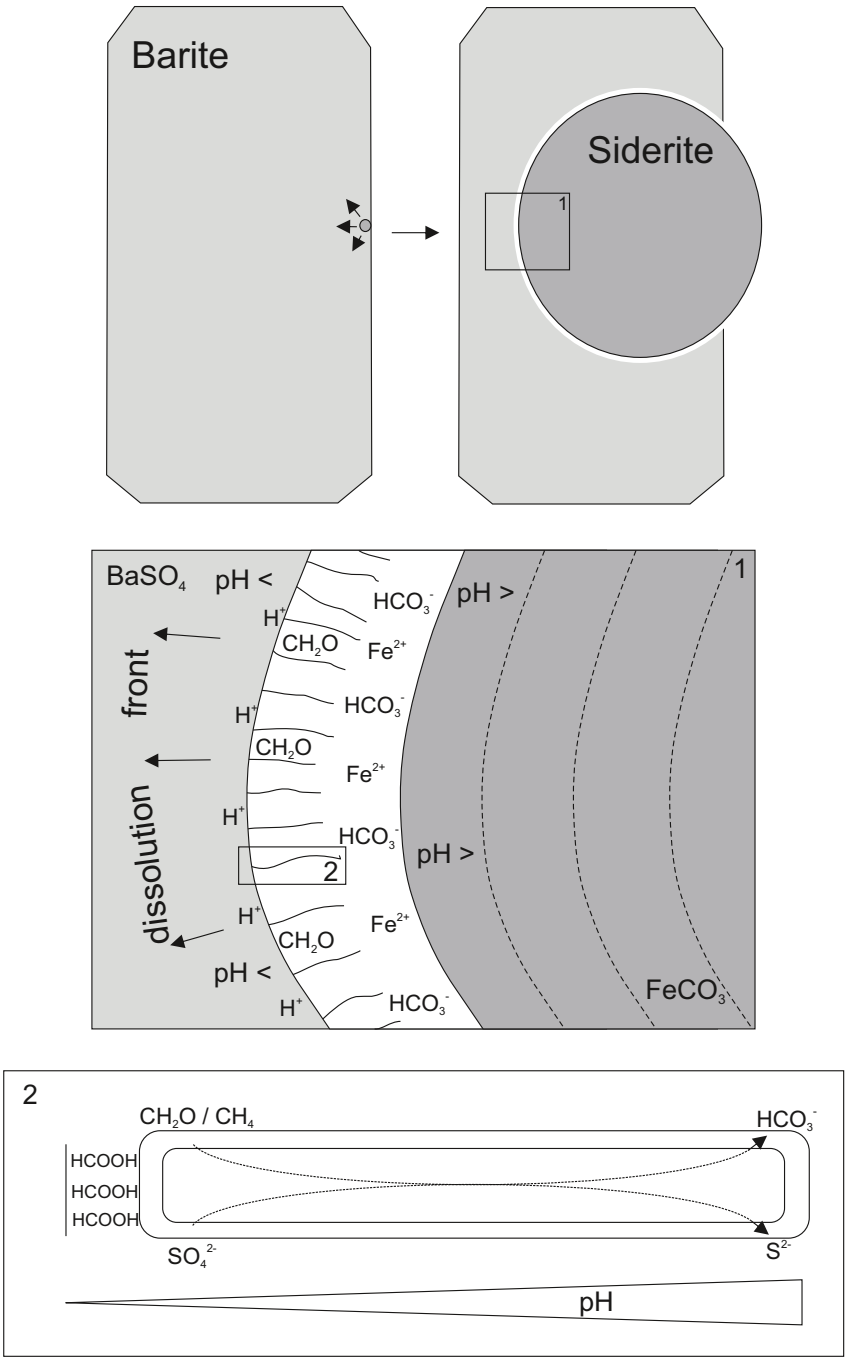

Figure 10